



City Research Online

City St George's, University of London

Citation: Li, H., Rane, S. & Yu, Z. (2021). Investigation of the performance and flow characteristics of two-phase reaction turbines in total flow geothermal systems. *Renewable Energy*, 175, pp. 345-372. doi: 10.1016/j.renene.2021.05.022

This is the published version of the paper.

This version of the publication may differ from the final published version. To cite this item please consult the publisher's version.

Permanent repository link: <https://openaccess.city.ac.uk/id/eprint/32429/>

Link to published version: <https://doi.org/10.1016/j.renene.2021.05.022>

Copyright and Reuse: Copyright and Moral Rights remain with the author(s) and/or copyright holders. Copies of full items can be used for personal research or study, educational, or not-for-profit purposes without prior permission or charge, unless otherwise indicated, provided that the authors, title and full bibliographic details are credited, a hyperlink and/or URL is given for the original metadata page and the content is not changed in any way. For full details of reuse please refer to [City Research Online policy](#).



Investigation of the performance and flow characteristics of two-phase reaction turbines in total flow geothermal systems



Hongyang Li ^a, Sham Rane ^b, Zhibin Yu ^{a,*}

^a James Watt School of Engineering, University of Glasgow, Glasgow, G12 8QQ, UK

^b Department of Engineering Science, University of Oxford, Oxford, OX2 0ES, UK

ARTICLE INFO

Article history:

Received 15 January 2021

Received in revised form

7 April 2021

Accepted 4 May 2021

Available online 7 May 2021

Keywords:

Two-phase turbine

Reaction turbine

Geothermal system

Flashing flow

Performance map

Trilateral cycle

ABSTRACT

In a total flow geothermal system, the two-phase turbine can generate output power and recover fresh water for the water-deficient area. The performance of the two-phase turbine under various working conditions is significantly affected by operation parameters of the geothermal system. This paper presented performance evaluation methods of two-phase turbines, including one-dimensional (1D) method, two-dimensional (2D) method and three-dimensional (3D) method. The 1D method was a fast iteration approach and could reflect average flow parameters along the impeller channel. The 2D method included nonuniform effects in the rotational direction and the 3D method could derive the complete 3D flow in the channel using CFD methods. The three models were validated with experimental results under various rotational speeds. Compared with the 3D method, the 1D method and the 2D method could significantly reduce computational time. The performance of the two-phase reaction turbine was evaluated under various working conditions. A correction method based on 1D and 3D results was proposed to generate the performance map and evaluate the influence of operation parameters of the geothermal system on the turbine performance. Proposed methods and analysis can be widely used in the design, selection and operation of two-phase reaction turbines for various thermal systems.

© 2021 The Authors. Published by Elsevier Ltd. This is an open access article under the CC BY license (<http://creativecommons.org/licenses/by/4.0/>).

1. Introduction

Geothermal resource is a clean and environmentally friendly sustainable energy, which can release the dependence of fossil fuels and reduce the emission of greenhouse gas. Due to its reliability, sustainability and high capacity factor [1], humans have a long history of exploiting geothermal resources [2]. The technological development of utilizing geothermal resources is crucial to the widespread introduction of geothermal power plants. Up to date, there are several ways of categorizing geothermal resources by various aspects, such as the temperature of reservoirs [3,4], the working fluid [5], geologic formations [6], the type of exploitation [7], and so on. Among them, hydrothermal systems have attracted extensive attention and studies.

Various thermodynamic cycles have been applied to hydrothermal systems, such as single-flash cycle, double-flash cycle, binary flash cycle, combined flash/binary cycle, Kalina cycle, and so on [8,9]. Cerci [10] studied exergy destructions in an 11.4 MW SFC

geothermal power plant in Turkey. Ozcan and Gokcen [11] concluded that the non-condensable gases were the most influencing factor on the performance of the single-flash cycle geothermal power plants. Zare and Palideh [12] used the thermoelectric generator instead of turbines to generate power in a Kalina cycle geothermal system. Acar and Arslan [13] stated that system efficiency was increased by about 1% when solar energy was integrated into the organic Rankine cycle geothermal system. Guzović et al. [14] developed a dual pressure organic Rankine cycle and performed energy and exergy analysis for Velika Ciglena geothermal power plant. However, introducing the organic Rankine cycle into geothermal plants brings higher capital costs to the investment than flash cycles.

The trilateral cycle was first introduced to flash circles by Smith [15] and could reduce the irreversible loss in the heat exchanger. The trilateral cycle was similar to the conventional flash circle except for the two-phase turbine. The inflow of the two-phase turbine was subcooled liquid or two-phase mixture. Due to the

* Corresponding author.

E-mail addresses: Hongyang.Li@glasgow.ac.uk (H. Li), sham.rane@eng.ox.ac.uk (S. Rane), Zhibin.Yu@glasgow.ac.uk (Z. Yu).

depressurization process of the fluid, there was remarkable phase-changing or flashing inside channels of two-phase turbines. However, conventional steam turbines or liquid turbines could not operate as two-phase turbines required by the trilateral cycle.

Two-phase turbines could be used in many industrial systems, such as oil and gas production [16], refrigeration [17–19], geothermal power [20,21], and so on, and classified into the impulse type and the reaction type. A two-phase impulse turbine consisted of two-phase nozzles and impellers. In two-phase nozzles, the fluid pressure was reduced to the outlet pressure of the turbine. Two-phase mixtures drove the impeller and generated shaft power. Elliot and Weinberg [22,23] presented detailed experimental studies about two-phase nozzles and rotors of the two-phase impulse turbine under various working fluids. Comfort and Beadle [20,24,25] measured a 20% efficiency single-stage two-phase impulse turbine for geothermal energy and concluded design considerations for two-phase turbines. Hays and Brasz [26,27] described the design and performance of the two-phase impulse turbine which was built in Manhattan. Cho et al. [19] investigated experimentally the performance of a two-phase impulse turbine used for air-conditioner and the total-to static efficiency of the turbine was 15.7% using R134a as the working fluid. He et al. [18] tested the performance of the twin-arc blade impeller using hydrofluorocarbons. Li et al. [28] carried out the design method of two-phase nozzles used for supercritical compressed air energy storage system. Friction loss and two-phase slip friction loss limited the peak efficiency of the two-phase impulse turbine.

A two-phase reaction turbine has a simple and reliable structure compared with the two-phase impulse turbine. Flow channels in the two-phase reaction turbine can be machined in a plate, and the impeller of the two-phase reaction turbine can be assembled directly on the shaft. There were several studies about two-phase reaction turbines in the past. Akagawa et al. [29,30] studied the performance of the two-phase nozzles and conducted experimental research of the two-phase reaction turbine using the air-water flow as the working fluid. In this paper, the inflow of the two-phase reaction turbine is subcooled water, the outlet flow of the two-phase turbine is vapour and liquid mixture, and the steam is generated in the channel since the outlet pressure is lower than the saturation pressure at the local temperature. Zhao et al. [31] and Date et al. [32] presented experimental research of the two-phase reaction turbine and stated the performance of the turbine under various working conditions. In this paper, performance evaluation methods were proposed based on one-dimensional flow equations and the CFD methods. Rane and He [33] presented the validation of mathematical models with experimental results proposed by Date et al. [32]. Rane and He [34] designed a novel geometry of the two-phase turbine using the numerical methods proposed in Ref. [33]. Li et al. [21] carried out a mean-line inverse design method for the two-phase reaction turbine. However, the inverse design method and the corresponding algorithm were only suitable for the design process and could not be employed to predict the distribution pressure and other flow parameters with the prescribed geometry.

In the two-phase reaction turbine, the erosion due to the accelerated flashing flow can degrade the performance of the turbine and even damage the impeller. The flashing erosion could occur in valves or orifices [35], and at the throat of the impeller in two-phase reaction turbines. The damage of the accelerated flashing flow to the throat can be mitigated in two ways, by using highly resistant materials or metal treatments, or by employing replaceable throats. Although the flashing erosion is usually referred to as “smooth” or “polished” [35,36], cavitation resistant materials and techniques for dealing with cavitation erosion could be applied for the flashing erosion, such as nickel-based cermet

coatings [37], plasma and gaseous nitriding treatments [38,39]. If the flashing erosion is limited strictly to the throat, the structure of the throat can be designed as a replaceable component. For example, Date et al. [40] designed several slots at different positions in the channel and inserted the orifice to study the effect of the nozzle configuration on the performance of the two-phase reaction turbine. In addition to the flashing erosion, the liquid impingement erosion can appear on the walls of the channel downstream the throat. The liquid impingement erosion can be avoided or alleviated by optimizing the shape and the curvature of the channel. It can be found that the erosion in the two-phase reaction turbine is highly dependent on the design of the channel and the performance evaluation of the impeller.

Few studies have been conducted about the performance evaluation of two-phase reaction turbines under various working conditions due to difficulties in predicting rotating flashing flow. Firstly, conventional evaluation methods are invalid for two-phase reaction turbines because of the flashing in the channel of the impeller. Secondly, thermal non-equilibrium effects, including the slip, the temperature difference between phases and the liquid attachment, make it difficult to evaluate the turbine performance. Thirdly, flow parameters at the inlet and the outlet are determined by the channel geometry and the flow process in the channel. Fourthly, the solving process of conservation equations is difficult to be converged because the vapour volume fraction increases almost from zero in the flashing flow. Liao and Lucas [41] reviewed the validation of various mathematical models for the simulation of the flashing flow in converging-diverging nozzles, and concluded that thermal phase change model could be more beneficial in predicting the flashing inception under significant thermal non-equilibrium effects. Rane and He [33,42] applied the thermal phase change model to simulate the flashing flow in the two-phase reaction turbine. There was the vapour layer generated on the wall near the throat and liquid attachment on the pressure side due to thermal non-equilibrium effects. Li et al. [21] proposed one-dimensional flashing flow equations to derive the geometry of the impeller with the prescribed distribution of pressure and relative flow angle, but the flow equations cannot be directly applied to the performance evaluation of the two-phase reaction turbine. Firstly, the divergence issues would arise in the algorithm, if the passage area was directly replaced by the pressure. Secondly, the algorithm could only be used under the design condition and was not able to evaluate the impeller performance under various working conditions. Thirdly, the method was a mean-line method based on one-dimensional flow assumptions along the flow direction and could not reflect the nonuniform effects in the rotational direction, such as the liquid attachment and secondary flow in the channel. Fourthly, the inverse design method cannot evaluate the influence of the system under various working conditions on the performance of two-phase reaction turbine.

In this paper, based on the mathematical models in the previous mean-line inverse-design method [21] and CFD analysis [42], performance evaluation methods and algorithms under various working conditions were presented. The 1D method was based on conservation equations and closure models for the two-phase flow presented by Li et al. [21] and the corresponding solving algorithm was proposed. The 2D approach was similar to the 3D method using CFD methods proposed by Rane et al. [42]. The three methods were validated using experimental results [32] and applied to evaluate the turbine performance under various working conditions. Section 2 describes the geometrical model and working conditions. In Section 3, mathematical models for the 1D and 2D/3D method are presented and CFD results are validated with the published experimental results. In Section 4, the performance of the two-phase reaction turbine under various working conditions are

discussed, and the influence of geothermal system parameters on the turbine performance is analyzed.

2. System and prototype turbine

2.1. Geothermal system adopted

The trilateral flash system [43] utilizes the total-flow turbine to convert the enthalpy of high-temperature liquid-dominated geothermal water to shaft power of the turbine. The discharge data of the geothermal fluid is from ‘LA-8’ heat source well in Aluto Langano geothermal field [44]. The geothermal system is shown in Fig. 1. The outflow from the production well may be the two-phase mixture or subcooled water, depending on the wellhead pressure. Yu et al. [43,45] discussed the influence of the wellhead pressure on the performance of the geothermal system. Due to environment and climate change, the wellhead pressure may be varied with years [46]. In the previous studies, the turbine efficiency is assumed to be a series of constants, and the performance of the turbine included only the working condition. The inlet pressure, rotational speed, inlet temperature and the inlet vapour volume fraction is of high influence on the performance of the turbine.

2.2. Prototype turbine

The structure of the two-phase turbine is shown in Fig. 2(a). The fluid from the production well flows into the impeller through a horizontal pipe of the turbine. The flow is distributed into each channel of the impeller and flashes into the two-phase mixture as shown in Fig. 2(b). The liquid and the vapour is separated in the casing of the turbine. The vapour leaves the turbine through the vapour outlet pipe installed on the top of the casing, and the liquid is discharged through the liquid outlet pipe installed at the bottom of the shell. For an impeller, the number of the channel can be chosen when the passage loss and the flow uniformity is considered. Fig. 2(c) and (d) show geometrical differences of impellers between six channels and two channels under the same total mass flow rate. If the number of the channel is too small, the large mass flow per channel and the cross-section area of the channel could be over large. The overlarge area can lead to dramatic changes in the curvature of the pressure line and the suction line. As shown in Fig. 2(d), because the mass flow per channel is much larger than that in Fig. 2(c), curvatures of the pressure line and suction line vary significantly along the flow direction. The excessive cross-section area and the rapid curvature change will lead to the failure of the performance evaluation method. However, the passage loss will be too large if there are too many channels. In this paper, an impeller with ten channels is studied.

The diagram of a single square-section channel is illustrated in Fig. 3, which is the projection of the channel on the plane normal to

the rotation direction. The basic shape of the channel is constructed by the center line, pressure line and suction line. The height of the cross section of the channel is equal to the width which can be derived by pressure line and suction line.

A mean-line inverse design method [21] is used to design the prototype turbine for the geothermal application. The inverse design method is different from the direct design method presented in the literature [32,33]. Using the inverse design method, a prototype turbine (PT) is designed, and the shape of the impeller is derived with the given pressure and blade angle distributions. The algorithm for this inverse method is similar to the inverse process of solving conservation equations. Parameters of the prototype turbine are listed in Table 1.

The inlet radius of the center line is 45.0 mm, the outlet radius is 188.5 mm, and the outlet radius of the pressure line is 200.0 mm. The geometry of the derived pressure line and suction line is shown in Fig. 4. At the throat, the width of the throat is 4.1 mm, the radius of the center line is 93.8 mm, the radius of the pressure line is 95.8 mm, and the radius of the suction line is 91.9 mm.

3. Methods and validation

3.1. One-dimensional model

3.1.1. Continuity, momentum and energy equations

An element for analyzing the one-dimensional flow is shown in Fig. 5. It has one inlet, one outlet and four walls, including the pressure side, the suction side, the top side and the bottom side. Flow parameters and thermophysical properties are assumed to be constant within the volume. Due to the rotation, the distribution of the pressure is different across the pressure side and the suction side. The pressure difference can be estimated approximately by the force balance on the direction normal to the center line. The 1D conservations and closure models are the same as the mathematical models presented by Li et al. [21].

There is no mass flux through the top side, the bottom side, the pressure side and the suction side. The continuity equation is built based on mass flux at the inlet and outlet, as illustrated in Equation (1).

$$\frac{d[\alpha A \rho_v W_v + (1 - \alpha) A \rho_l W_l]}{dL} = 0 \tag{1}$$

The momentum equation is built based on the balance of the force exerted on the element along the center line and can be expressed as

$$\frac{d[\alpha A \rho_v W_v^2 + (1 - \alpha) A \rho_l W_l^2]}{dL} = -A \frac{dP}{dL} - A \left(\frac{dP}{dL} \right)_f + A[\alpha \rho_v + (1 - \alpha) \rho_l] \Omega^2 R \cos \gamma \tag{2}$$

According to the first law of thermodynamics, the energy equation of the total flow can be derived as Equation (3) along the center line. The velocity in turbomachinery is so high that the fluid has no time to exchange heat with the surrounding [47]. The flow in most turbines could be assumed to be adiabatic [48–51], but the internal heat transfer in turbochargers and small gas turbines affects the performance operating point of the turbocharger or gas turbine [52]. The temperature difference in the two-phase turbine is much lower than that in the turbocharger or gas turbine. Furthermore, the flashing models were commonly assumed to be adiabatic [53] and the flashing flow was often referred as the adiabatic flash. Therefore, the heat flux across the walls of the channel is neglected and the two-phase flow is assumed to be adiabatic in this paper.

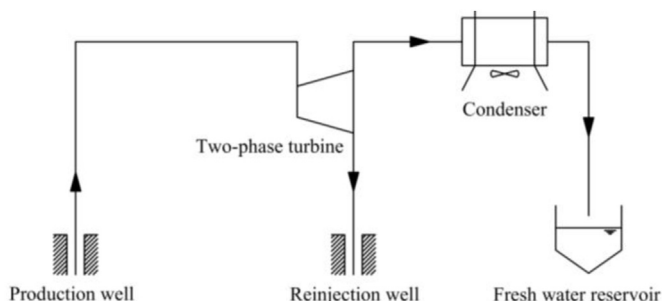


Fig. 1. Diagram of the total flow system [43].

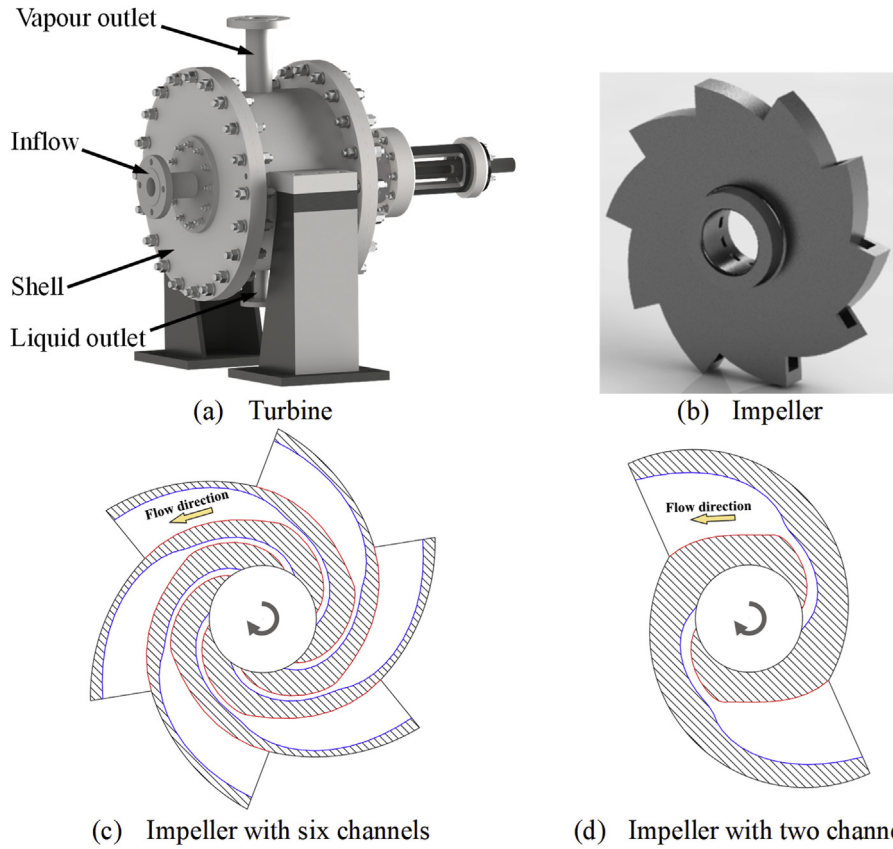


Fig. 2. The geometry model of the two-phase reaction turbine.

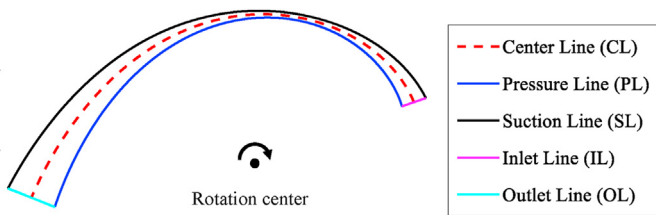


Fig. 3. Curves in a single channel.

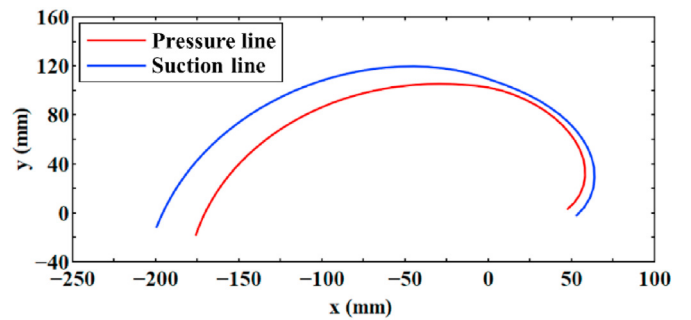


Fig. 4. The pressure line and suction line of a single channel.

Table 1
Parameters of the designed turbine.

Parameter	Value
Inlet pressure	1.1 MPa
Inlet temperature	174 °C
Outlet pressure	0.1 MPa
Mass flow rate per impeller	5 kg/s
Number of channels per impeller	10
Number of impellers in the turbine	2
Rotational speed	2200 rpm

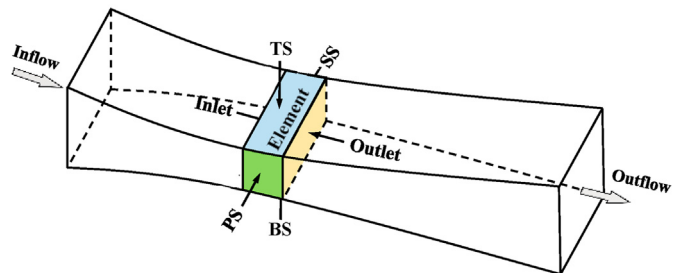


Fig. 5. Element for one-dimensional analysis.

$$\frac{dE_{mixture}}{dL} = -\frac{dP_{of}}{dL} \quad (3)$$

with

$$\begin{cases} \frac{dP_o_f}{dL} = A[\alpha W_v + (1 - \alpha)W_l] \left(\frac{dP}{dL}\right)_f dL \\ E_{mixture} = \alpha A \rho_v W_v \left(H_v + \frac{W_v^2 - U^2}{2}\right) + (1 - \alpha) A \rho_l W_l \left(H_l + \frac{W_l^2 - U^2}{2}\right) \end{cases} \quad (4)$$

3.1.2. Force balance equation of vapour bubble

The slip between the liquid and the vapour can be derived as Equation (5) based on the balance of the force exerted on a sphere bubble along the center line. The increase of the momentum should be balanced with the pressure reduction, centrifugal force and drag force.

$$\begin{aligned} \frac{\pi D^3}{6} \rho_v W_v \frac{dW_v}{dL} = & -\frac{\pi D^2}{4} \frac{dP}{dL/D} - \frac{\pi D^2}{8} C_D (W_v - W_l) |W_v - W_l| \\ & + \frac{\pi D^3}{6} \rho_v N^2 R \cos \gamma \end{aligned} \quad (5)$$

with

$$D = \left(\frac{6\alpha}{\pi D_n}\right)^{\frac{1}{3}} \quad (6)$$

Equation (5) should be implemented into Equation (2) to solve the vapour velocity and the liquid velocity.

3.1.3. Phase-changing model

The flashing flow in the channel is caused by thermodynamic and mechanical nonequilibrium. The thermal phase-changing model has been validated with experimental results by Rane et al. [54] for the two-phase reaction turbine. The interphase mass flux can be modelled with Equation (7).

$$\Gamma = A_{ia} \frac{Q}{H_l - H_v} \quad (7)$$

where A_{ia} is the interfacial area density. The heat flux of a single sphere bubble in the liquid is used to construct the thermodynamic model of the flashing. The heat flux between the two-phase fluids is

$$Q = h_{int}(T_l - T_v) \quad (8)$$

where h_{int} is the heat transfer coefficient and can be calculated using Nusselt number. Wolfert [55] proposed a model to correlate Nusselt number with thermodynamic and mechanical nonequilibrium as

$$Nu = \frac{12}{\pi} Ja_T + 2\sqrt{\frac{Pe}{\pi}} \quad (9)$$

where Ja_T is Jacob number and Pe is Peclet number. They can be evaluated using Equations (10) and (11).

$$Ja_T = \frac{\rho_l C_{p_l} \max(T_l - T_{sat}, 0)}{\rho_g L} \quad (10)$$

$$Pe = \frac{D|V_v - V_l|}{\gamma_l} \quad (11)$$

3.1.4. Frictional pressure reduction model

There are several empirical equations [56,57] used to evaluate the two-phase frictional pressure reduction in Equation (2). Many of those equations only consider water and air mixture. However, the correlation from Ref. [58] is suitable for a single component and expressed as

$$\left(\frac{dP}{dL}\right)_f = \Phi \left(\frac{dP}{dL}\right)_{f,lo} \quad (12)$$

where Φ is an empirical parameter used to evaluate the effect of the two-phase flow. The detailed formula for Φ can be referenced to Ref. [58].

3.2. Three-dimensional model

3.2.1. Continuity, momentum and energy equations

In a rotating reference frame system, the continuity equations are written as

$$\begin{cases} \frac{\partial}{\partial t}(\alpha \rho_v) + \nabla \cdot (\alpha \rho_v \vec{W}_v) = \Gamma \\ \frac{\partial}{\partial t}[(1 - \alpha)\rho_l] + \nabla \cdot [(1 - \alpha)\rho_l \vec{W}_l] = -\Gamma \end{cases} \quad (13)$$

where $\vec{W} = \vec{V} + \vec{\Omega} \times \vec{r}$. The momentum equations read as

$$\begin{cases} \frac{\partial}{\partial t}(\alpha \rho_v \vec{W}_v) + \nabla \cdot (\alpha \rho_v \vec{W}_v \vec{W}_v) = -\alpha \nabla P + \vec{F}_v^t + \vec{F}_v^g \\ \quad + \vec{F}_v^d + \vec{F}_v^{int} - \alpha \rho_v [\vec{\Omega} \times (\vec{\Omega} \times \vec{R})] - 2\alpha \rho_v (\vec{\Omega} \times \vec{W}_v) \\ \frac{\partial}{\partial t}[(1 - \alpha)\rho_l \vec{W}_l] + \nabla \cdot [(1 - \alpha)\rho_l \vec{W}_l \vec{W}_l] = -(1 - \alpha) \nabla P \\ \quad + \vec{F}_l^t + \vec{F}_l^g + \vec{F}_l^d + \vec{F}_l^{int} - (1 - \alpha)\rho_l [\vec{\Omega} \times (\vec{\Omega} \times \vec{R})] \\ \quad - 2(1 - \alpha)\rho_l (\vec{\Omega} \times \vec{W}_v) \end{cases} \quad (14)$$

The energy equations are expressed by

$$\begin{cases} \frac{\partial}{\partial t}(\alpha \rho_v H_v) + \nabla \cdot (\alpha \rho_v \vec{W}_v H_v) = \nabla \cdot (\alpha \phi_v \nabla T_v) + Q_v^{int} + Q_v^t \\ \frac{\partial}{\partial t}[(1 - \alpha)\rho_l H_l] + \nabla \cdot [(1 - \alpha)\rho_l \vec{W}_l H_l] = \nabla \cdot [(1 - \alpha)\phi_l \nabla T_l] \\ \quad + Q_l^{int} + Q_l^t \end{cases} \quad (15)$$

3.2.2. Turbulence model

In the converging section of the channel, the fluid is mainly

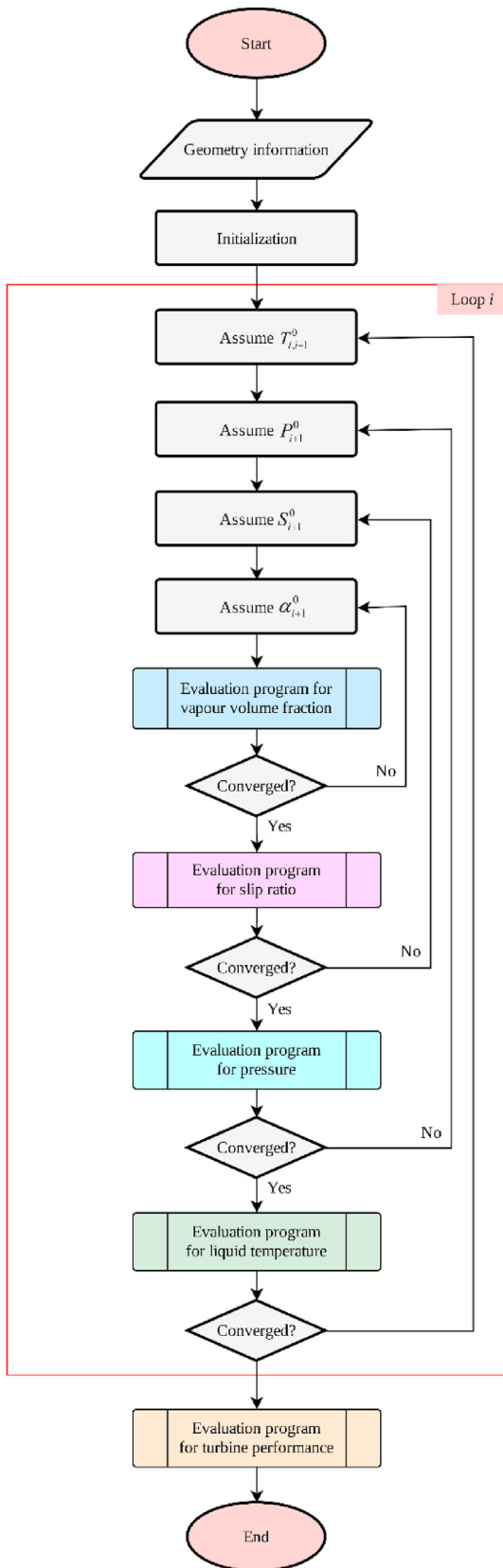


Fig. 6. Flow chart of the 1D method.

composed of the liquid water and the flow speed is low. In the diverging section, both the mixing process and separating process

of liquid and vapour exist, and the mixture flow velocity increases significantly. The area of the throat is so narrow that the boundary layer grid near the throat can be very thin. The turbulence model is based on the $k-\epsilon$ and $k-\omega$ models [59].

For the rotating reference frame system, the turbulence should be modified using the empirical function. Detailed correction is introduced in Ref. [60]. Although kinetic energy and dissipation of turbulent energy are different between the vapour and the liquid, the homogenous turbulent model is used in this paper.

3.2.3. Drag force equation on bubble

For a single bubble in the flow, the drag force in Equation (14) can be derived as

$$\bar{F}^{-d} = \frac{1}{2} C_D \rho_l |V_v - V_l| (V_v - V_l) A_p \quad (16)$$

where A_p is the projected area of the bubble in the flow. In the unit volume, the drag force is

$$\bar{F}^{-d} = \frac{3}{4D} C_D \alpha \rho_l |V_v - V_l| (V_v - V_l) \quad (17)$$

where D is the bubble diameter.

Vapour properties are set as saturation vapour properties using the local pressure. Liquid properties are calculated by checking IAPWS. The phase-changing model for the 1D model can be still used for the 2D and 3D models.

3.3. Methods and algorithm

3.3.1. 1D method

The presented algorithm is shown in Fig. 6 and programmed in Python. Given boundary conditions include inlet pressure, inlet temperature, inlet volume fraction, rotational speed and outlet pressure. In the 1D element, flow parameters at node $i+1$ can be solved using parameters at node i . The conservation equations are solved with a coupled method.

The algorithm for solving 1D equations needs special concern. Firstly, large error and severe numerical divergence may appear near the inception point of the flashing, because the vapour volume fraction increases from the minimum vapour volume fraction, and strange values of vapour velocity can be derived if the vapour velocity is solved directly from the momentum conservation equation or the continuity equation. Secondly, there may be multiple solutions during the solving process for the pressure. Thirdly, the under-relaxation factor significantly affects the accuracy and robustness of the algorithm, and the initialization field determines whether the solving process is converged. Thus, in the presented algorithm the vapour velocity is calculated indirectly by using the derived liquid velocity and slip ratio, and the pressure is evaluated using the liquid density. It should be noted that the pressure can also be derived through rearranging the momentum conservation equation and continuity equation.

Compared with the algorithm in the previous inverse design method [21], programs for the centerline and inlet section are unnecessary because the geometry of the channel has been provided. The passage area is a given parameter, and the pressure needs to be solved, as shown in Fig. 7. Thus, modifications should be made in many subprograms especially in evaluation program for the pressure. The passage area is derived mainly using the continuity equation in the inverse design method. But in this paper, the density is derived through the continuity equation and then the corrected pressure is calculated using the saturation property of the fluid. The sequence for solving discretized conservation equations

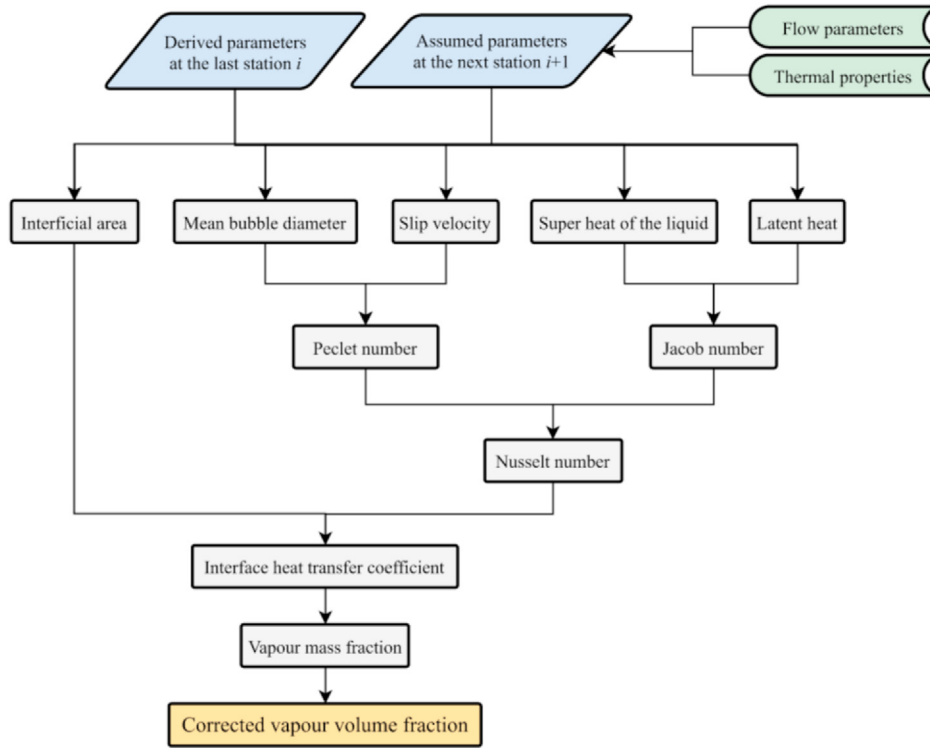


Fig. 7. Flow chart of the evaluation program for the vapour volume fraction.

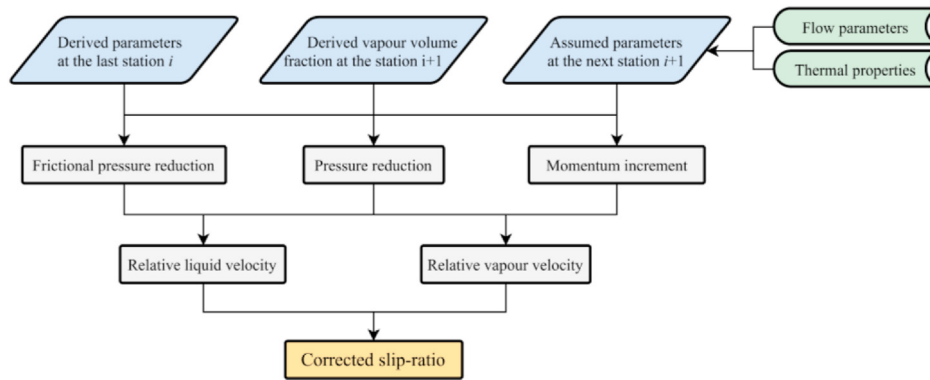


Fig. 8. Flow chart of the evaluation program for slip-ratio.

and closure equations should be also rearranged. The slip ratio is solved after the passage area is determined in the inverse design method, but it is calculated before the pressure is evaluated to avoid the divergence of the algorithm in this algorithm. The initialization

affects the convergence remarkably in this algorithm, so the distribution of flow parameters obtained by the inverse-design method is employed to initialize this algorithm.

In the evaluation program for the vapour volume fraction, the

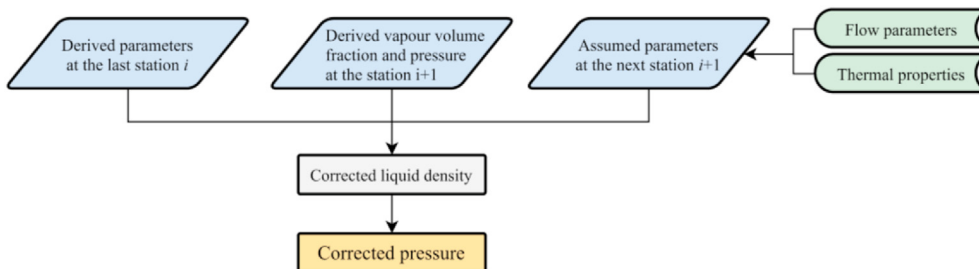


Fig. 9. Flow chart of the evaluation program for pressure.

phase-changing equation is mainly solved using the procedure shown in Fig. 5. Firstly, thermophysical properties should be averaged between computation nodes i and $i+1$. Secondly, the velocity at node $i+1$ should be used to derive the slip velocity between the two-phases. Thirdly, the temperature at node $i+1$ should be used to calculate the superheat of the liquid. Fourthly, the vapour volume fraction at node $i+1$ should be used to evaluate the mean bubble diameter.

The procedure for calculating the slip ratio is shown in Fig. 8. Firstly, the relative liquid velocity is evaluated using rearranged momentum equation as illustrated in Equations (18) and (19). Secondly, the relative vapour velocity is derived using the rearranged slip equation as shown in Equation (20). Thirdly, the corrected slip ratio is calculated.

The rearranged discretized momentum conservation equation is

$$W_{l,i+1}^* = \frac{1}{m_{l,i+1}} \left\{ M_i - \left[(P_{i+1}^0 - P_i) + \left(\frac{dP}{dL} \right)_f dL - Q^2 R_{i+\frac{1}{2}} dL \rho_m \cos \gamma_{i+\frac{1}{2}} \right] A_{i+\frac{1}{2}} - m_{v,i+1} W_{v,i+1}^0 \right\} \quad (18)$$

with

$$M_i = m_{l,i} W_{l,i} + m_{v,i} W_{v,i} \quad (19)$$

It should be noted that there may be other ways for any variable φ , $\varphi_{i+1/2}$ means $(\varphi_i + \varphi_{i+1})/2$. The rearranged discretized slip equation is

$$W_{v,i+1}^* = W_{l,i} + W_{l,i+1}^* - W_{v,i\pm 2} \sqrt{\left| \frac{\Pi_1 + \Pi_2 + \Pi_3}{\Pi_4} \right|} \quad (20)$$

with

$$\left\{ \begin{aligned} \Pi_1 &= -\frac{\pi}{6} D_{i+\frac{1}{2}}^3 \rho_{v,i+\frac{1}{2}} \frac{(W_{v,i+1}^0)^2 - (W_{v,i})^2}{L_{i+1} - L_i} \\ \Pi_2 &= -\frac{\pi}{4} D_{i+\frac{1}{2}}^3 \frac{P_{i+1} - P_i}{L_{i+1} - L_i} \\ \Pi_3 &= \frac{\pi}{6} D_{i+\frac{1}{2}}^3 \rho_{v,i+\frac{1}{2}} Q^2 R_{i+\frac{1}{2}} \cos \gamma_{i+\frac{1}{2}} \\ \Pi_4 &= \frac{\pi}{8} D_{i+\frac{1}{2}}^2 C_D \end{aligned} \right. \quad (21)$$

The sign of Equation (20) is decided by the sign of $(\Pi_1 + \Pi_2 + \Pi_3)/\Pi_4$.

The corrected pressure is evaluated indirectly through the continuity equation, as shown in Fig. 9. Firstly, the corrected liquid density can be derived by rearranging continuity equation. Secondly, the corrected pressure is evaluated by checking the saturation curve. The rearranged continuity equation is

$$\rho_{l,i+1}^* = \frac{m - \rho_{v,i+1}^0 \alpha_{i+1}^* W_{v,i+1}^*}{W_{l,i+1}^* (1 - \alpha_{i+1}^*)} \quad (22)$$

Using the saturation data from IAPWS, the saturation curve can be fitted as

$$P = c_0 + c_1 \cos(\rho_l w) + c_2 \sin(\rho_l w) + c_3 \cos(2\rho_l w) + c_4 \sin(2\rho_l w) \quad (23)$$

with $c_0 = -476.4$, $c_1 = -9801$, $c_2 = -1349$, $c_3 = 871$, $c_4 = -4836$ and $w = 0.004714$. It should be noted that Equation (23) can only be valid when the pressure is between 1 kPa and 1.5 MPa, and the unit of the derived pressure is kPa.

The corrected liquid temperature can be derived by solving the energy conservation equation. The energy conservation equation can be arranged as

$$T_{l,i+1}^* = \frac{1}{C_{p,l,i+\frac{1}{2}}} \left[\frac{(I_{v,i} + I_{l,i} - P_{of,i} - I_{v,i+1})}{m_{l,i+1}} - \frac{W_{l,i+1}^2 - U_{i+1}^2}{2} \right] + T_{l,i} \quad (24)$$

with

$$\left\{ \begin{aligned} I_{v,i} &= m_{v,i} \left(H_{v,i} + \frac{W_{v,i}^2 - U_i^2}{2} \right) \\ I_{l,i} &= m_{l,i} \left(H_{l,i} + \frac{W_{l,i}^2 - U_i^2}{2} \right) \end{aligned} \right. \quad (25)$$

where I is the rthalpy as illustrated in Ref. [61]. The friction loss can be derived by using the frictional pressure reduction, which has already been calculated in the evaluation program of slip-ratio.

The turbine performance, especially the output power, can be evaluated by the pressure distribution on four boundaries of the channel and the friction loss. The output power includes three items as

$$Po = \sum_{i=1}^n To_{p,i+\frac{1}{2}} \Omega B_N + \sum_{i=1}^n To_{f,i+\frac{1}{2}} \Omega B_N + To_{out} \Omega B_N \quad (26)$$

where n is the total number of computational stations, B_N is the total number of channels, Ω is the rotational speed, To_f is the torque caused by the two-phase flow friction, To_p is the torque caused by the pressure, and To is the torque. The torque at the outlet can be derived as

$$To_{out} = \iint_{A_{out}} R_{out}(x,y) \sin|\gamma(x,y)| P_{out} dA(x,y) \quad (27)$$

The pressure on the pressure line and the suction line can be evaluated using the simple radial equilibrium principle by Li et al. [21]. The torque caused by the pressure can be calculated by

$$\begin{aligned} To_{p,i+\frac{1}{2}} &= F_{x,i+\frac{1}{2}}^{PS} y_{i+\frac{1}{2}}^{PL} - F_{y,i+\frac{1}{2}}^{PS} x_{i+\frac{1}{2}}^{PL} + F_{x,i+\frac{1}{2}}^{SS} y_{i+\frac{1}{2}}^{SL} - F_{y,i+\frac{1}{2}}^{SS} x_{i+\frac{1}{2}}^{SL} + F_{x,i+\frac{1}{2}}^{TS} y_{i+\frac{1}{2}}^{CL} \\ &\quad - F_{y,i+\frac{1}{2}}^{TS} x_{i+\frac{1}{2}}^{CL} + F_{x,i+\frac{1}{2}}^{BS} y_{i+\frac{1}{2}}^{CL} - F_{y,i+\frac{1}{2}}^{BS} x_{i+\frac{1}{2}}^{CL} \end{aligned} \quad (28)$$

with

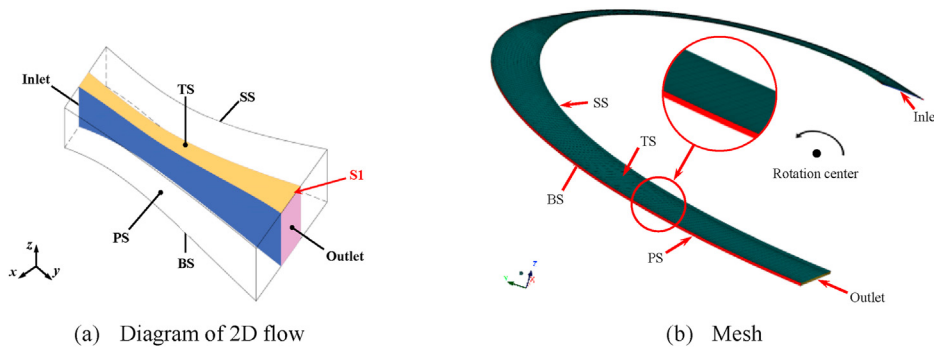


Fig. 10. Diagram of 2D flow and mesh for the 2D method.

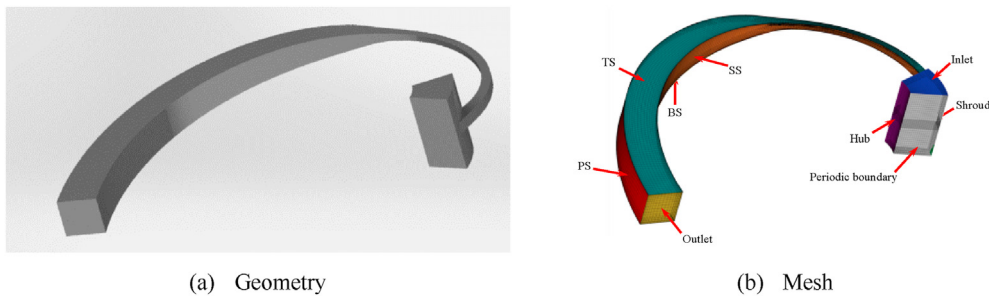


Fig. 11. Geometry and mesh model for the 3D method.

$$\begin{cases}
 F_{x,i+\frac{1}{2}}^{PS} = P_{i+\frac{1}{2}}^{PL} Z_{i+\frac{1}{2}} (L_{i+1}^{PL} - L_i^{PL}) \cos\left(\beta_{i+\frac{1}{2}} - \frac{\pi}{2}\right) \\
 F_{y,i+\frac{1}{2}}^{PS} = P_{i+\frac{1}{2}}^{PL} Z_{i+\frac{1}{2}} (L_{i+1}^{PL} - L_i^{PL}) \sin\left(\beta_{i+\frac{1}{2}} - \frac{\pi}{2}\right) \\
 F_{x,i+\frac{1}{2}}^{SS} = -P_{i+\frac{1}{2}}^{SL} Z_{i+\frac{1}{2}} (L_{i+1}^{SL} - L_i^{SL}) \cos\left(\beta_{i+\frac{1}{2}} - \frac{\pi}{2}\right) \\
 F_{y,i+\frac{1}{2}}^{SS} = -P_{i+\frac{1}{2}}^{SL} Z_{i+\frac{1}{2}} (L_{i+1}^{SL} - L_i^{SL}) \sin\left(\beta_{i+\frac{1}{2}} - \frac{\pi}{2}\right)
 \end{cases} \quad (29)$$

The torque caused by the friction can be evaluated as

$$T_{f,i+\frac{1}{2}} = F_{f,x,i+\frac{1}{2}} y_{i+\frac{1}{2}}^{CL} - F_{f,y,i+\frac{1}{2}} x_{i+\frac{1}{2}}^{CL} \quad (30)$$

with

$$\begin{cases}
 F_{f,x,i+\frac{1}{2}} = -\left(\frac{dP}{dL}\right)_{f,i+\frac{1}{2}} (L_{i+1}^{CL} - L_i^{CL}) A_{i+\frac{1}{2}} \cos\left(\beta_{i+\frac{1}{2}} - \frac{\pi}{2}\right) \\
 F_{f,y,i+\frac{1}{2}} = -\left(\frac{dP}{dL}\right)_{f,i+\frac{1}{2}} (L_{i+1}^{CL} - L_i^{CL}) A_{i+\frac{1}{2}} \sin\left(\beta_{i+\frac{1}{2}} - \frac{\pi}{2}\right)
 \end{cases} \quad (31)$$

The turbine efficiency is defined as ratio between the output power of the impeller and the isentropic output power as shown in Equation (32).

$$\eta = \frac{Po}{m(H^{in} - H^{out})} \times 100\% \quad (32)$$

3.3.2. 2D and 3D methods

The algorithms for 2D and 3D methods are the same, but the mesh, boundary conditions and numerical settings are different. The 2D geometrical model of the channel is shrunk from 3D geometry model using a scale factor in the span direction (z-direction or height direction). To allow ANSYS CFX to eliminate the z-direction flow, there is only one layer of the mesh in the z-direction, and both the top side and the bottom side are subject to the symmetrical boundary condition. The vector parallel tolerance is 2° to allow curved symmetric surfaces and increases with the scale factor. There is a balance between the accuracy and the convergence,

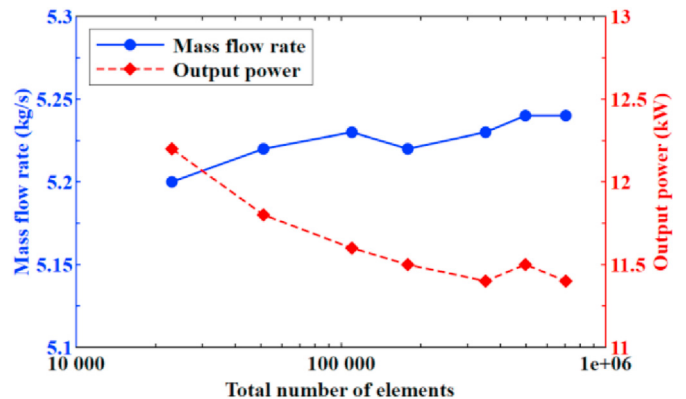
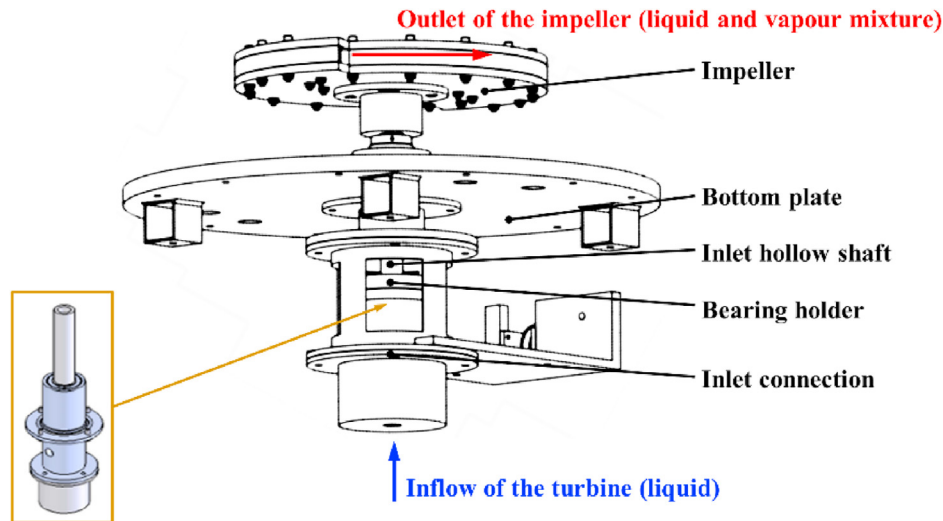
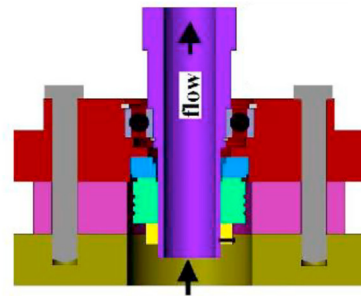


Fig. 12. Performance of the impeller under different numbers of elements.



(a) Diagram of the flow path



(b) Structure of the turbine near the inlet

Fig. 13. Diagram of RMIT turbine [32,64,65].

because a necessary vector parallel tolerance may reduce the accuracy of 2D evaluation method.

In this paper, the Euler-Euler method is chosen to simulate the flashing flow using ANSYS CFX. The thermophysical properties of the vapour are calculated using IAPWS. The coupled algorithm is used to increase the robustness of the simulation and can be referenced to Ref. [60]. The liquid is the continuous phase while its vapour is the dispersed phase. The mean bubble diameter should be changed based on the local vapour volume fraction using Equation (6). The bubble number density is set to be 5×10^7 , which is validated by Rane and He [33]. The turbulence model is homogenous $k-\omega$ model since it is suitable for bubbly flow according to the validation by Ibrahim et al. [62]. The steady solver is used in the simulation with the upper limit of the time scale factor 10^{-5} s. IAPWS IF97 is imported to the simulation as well. The initial flow field is of significant influence on the convergence of the solving process. Rane and He [33] presented equations for the initialization. In this paper, the initial pressure and the vapour volume fraction are given by the 1D results. The rotational speed of the computation domain increases from zero to the designed rotational speed with growing iteration step of the simulation.

3.3.3. Geometrical models and mesh size independence in 2D and 3D methods

In the 2D method, the flow on the relative flow stream surface S1 is predicted while the flow on the stream surface S2 is uniform based on the general 3D fluid dynamics in turbomachinery

proposed by Wu [63], as illustrated in Fig. 10(a). There is only one element in the z -direction as shown in Fig. 10(b). The scale factor in the z -direction τ_z is 0.04, and the mass flow rate and the torque obtained by the 2D model should be scaled based on the scale factor.

The geometrical model for the 3D method is one-tenth of the whole channel to reduce the computation cost, as shown in Fig. 11(a). ICEM is used to generate the structural mesh as illustrated in Fig. 11(b). A periodic boundary conditions is imposed in the inlet tube of the impeller. The first distance from the wall in the flow channel is 0.1 mm and the growth rate is 1.2.

The performance of the turbine includes the flow rate, the output power, and the pressure difference. The mesh dependency of the channel is studied as illustrated in Fig. 12. The result shows that in the current settings the performance of the turbine is not sensitive to the amount of the mesh. In this paper, the total number of the mesh is chosen as 179 k.

3.4. Validation of the methods with experimental results

Experimental results of a two-phase reaction turbine (the turbine is named RMIT turbine and its impeller is named as RMIT impeller) was published by Date et al. [32], and the detailed structure of the turbine was presented by Khaghani [64] as shown in Fig. 13(a). The inflow of Date's turbine flows into a hollow shaft and is guided into the impeller. The two-phase outflow leaves the impeller into the case of the turbine. Gaps between rotational parts

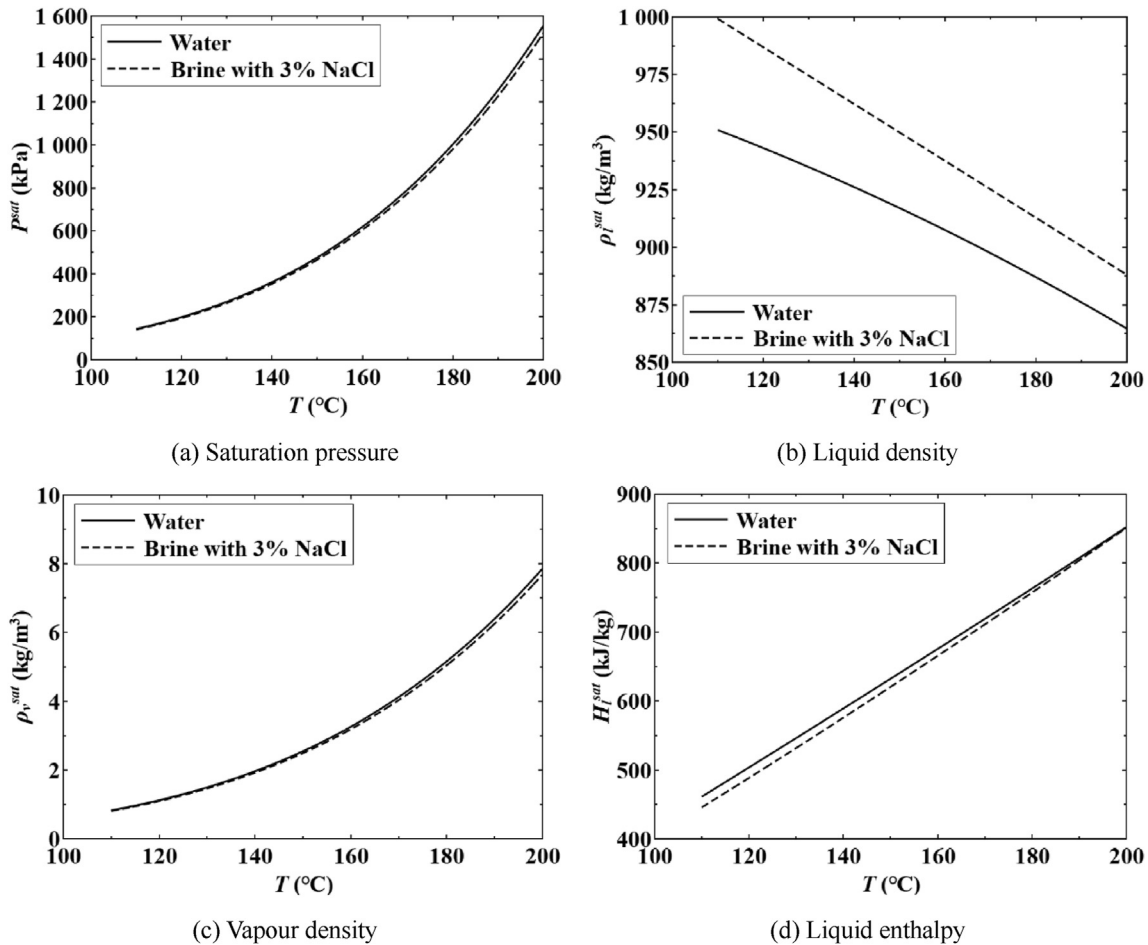


Fig. 14. Comparison of thermophysical properties between the water and the brine with 3% NaCl.

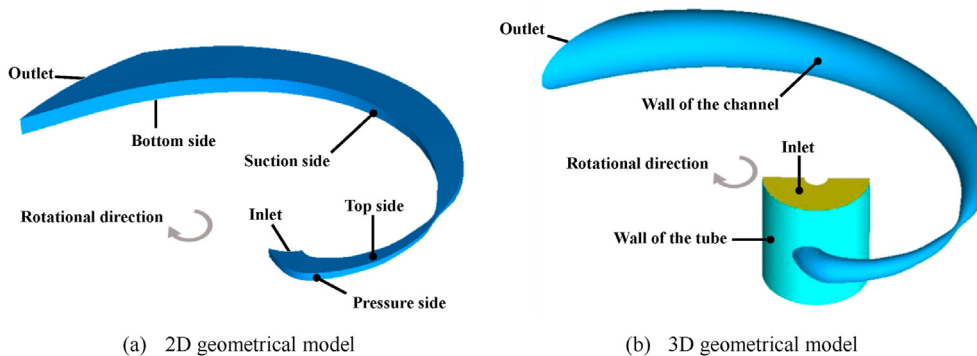


Fig. 15. Geometry model and performance of RMIT impeller's impeller.

and stationary parts are sealed by mechanical seals [65], as shown in Fig. 13(b). Thus, the flow rate through gaps is neglected in the simulation due to the low leakage. However, the usage of the mechanical seal brings additional friction loss to the turbine. Date et al. [40] monitored deceleration rate of the turbine after stopping the feed water supply and derived the output power of the shaft while the frictional loss of the mechanical seal and bearings was deduced.

The performance of the two-phase turbine varies with the salt content. In the previous experiment, the inflow is the saltwater and contains 3% NaCl. Thermophysical properties vary with the salt content in the NaCl–H₂O mixture, including the saturation

pressure, the density, the viscosity, and so on. The relationship between the saturation pressure and the salt content can be illustrated in Equation (33).

$$P_{\text{brine}} = aP_{\text{water}} \tag{33}$$

where P_{water} is the saturation pressure for the water, P_{brine} is the saturation pressure for the brine, and the coefficient a in Equation (33) decreases as the salt content increases and can be fitted as Equation (34) using the published data [66] when the temperature varies from 110 °C to 330 °C.

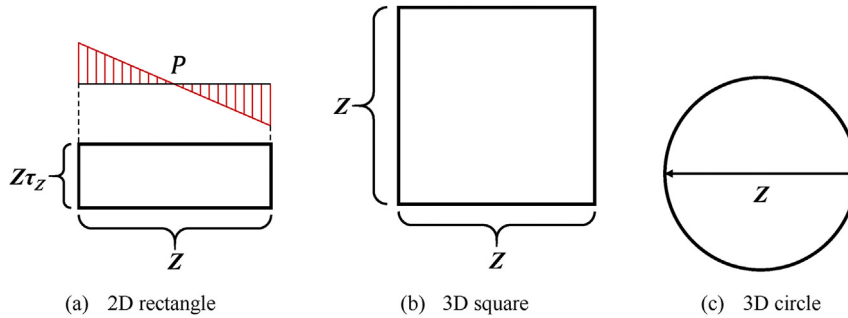


Fig. 16. Diagram of the cross-section for 2D simulation and 3D simulation.

$$a = -1.129c^2 - 0.5384c + 0.995 \quad (34)$$

where c is the salt content. If c is 0.03, a is 0.9778. The saturation pressure of the brine and the water can be illustrated in Fig. 14(a). The deviation of the saturation pressure between the 3% NaCl mixture and the water increases with the temperature and is 34.5 kPa when the temperature is 200 °C. The liquid brine density is higher than the liquid water density and the deviation of the liquid density between the brine and the water increases with the salt content. Using the published data [66], the maximum deviation of the liquid density is 48.34 kg/m³ in Fig. 14(b), the maximum deviation of the vapour density is 0.17 kg/m³ in Fig. 14(c), and the maximum deviation of the liquid enthalpy is 1.24 kJ/kg in Fig. 14(d), if the temperature varies between 110 °C and 200 °C. Thus, in this paper, the water has been chosen as the working fluid in the simulation for simplicity, because deviations of thermophysical properties are not significant within the temperature range studied.

There are several geometrical differences between the RMIT impeller and the prototype turbine's impeller of this research. Firstly, the RMIT impeller has two channels and the prototype turbine's impeller has ten channels. Secondly, the cross-section normal to the center line of the RMIT impeller is circle and the prototype turbine's impeller has a square channel, as shown in Figs. 11(a) and Figure 15(b). Thirdly, the RMIT impeller has an outlet section which is the extension of the main channel, and the prototype turbine's impeller doesn't have a similar outlet section. Fourthly, RMIT impeller has two parts which are symmetric by $z = 0$ mm plane. The two parts are assembled into the impeller by several bolts. The prototype turbine's impeller has a whole channel which is manufactured using the 3D printing technique. Fifthly, the

RMIT impeller and the prototype turbine's impeller have different geometry and working conditions. However, mathematical models and parameters for the three models are suitable for both the RMIT impeller and the prototype turbine's impeller. The 1D model and 2D model are established based on the rectangle cross-section. If the 1D model and 2D model are applied to the RMIT impeller, the area calculation and the evaluation program of the output power should be modified. For the 2D geometry model, the cross-section of the channel is rectangle as illustrated in Fig. 15(a).

The height of the channel along the center line in the 2D model is equal to the distribution of the scaled radius in the 3D model. The flow rate obtained by the 2D model should be corrected using the scale factor τ_z and the area factor, which is the area ratio between the rectangle and the circle. The output power obtained by the 2D model is modified using the scale factor τ_z and the shape factor τ_s . For either 2D or 3D simulation, the output power of the channel can be divided into three parts as

$$P_o = P_o^{PS+SS} + P_o^{TS+BS} + P_o^{Outlet} \quad (35)$$

where $P_o^{Outlet} = 0$ because the outlet of the impeller has a constant radius. Thus, it can be found that the output power is strongly affected by the geometry of the pressure side, suction side, top side and bottom side. The shape factor should be derived using the relationship between the 2D and 3D geometry.

The 2D output power derived directly is not the 3D output power since the cross-section is different between the 2D and the 3D. The geometry of the 2D is a rectangle, as shown in Fig. 16(a). For 2D simulation, the width of the cross-section Z is equal to that of 3D cross-section. The height of the 2D cross-section is equal to $Z\tau_z$. In order to correlate the 2D output power to the 3D output power, the 2D rectangular cross-section is firstly scaled to the 3D square cross-

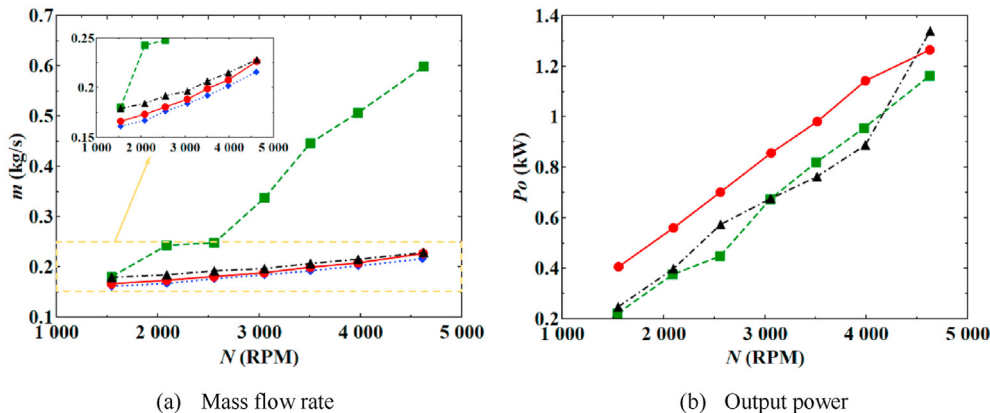


Fig. 17. Geometry model and performance of the RMIT's impeller.

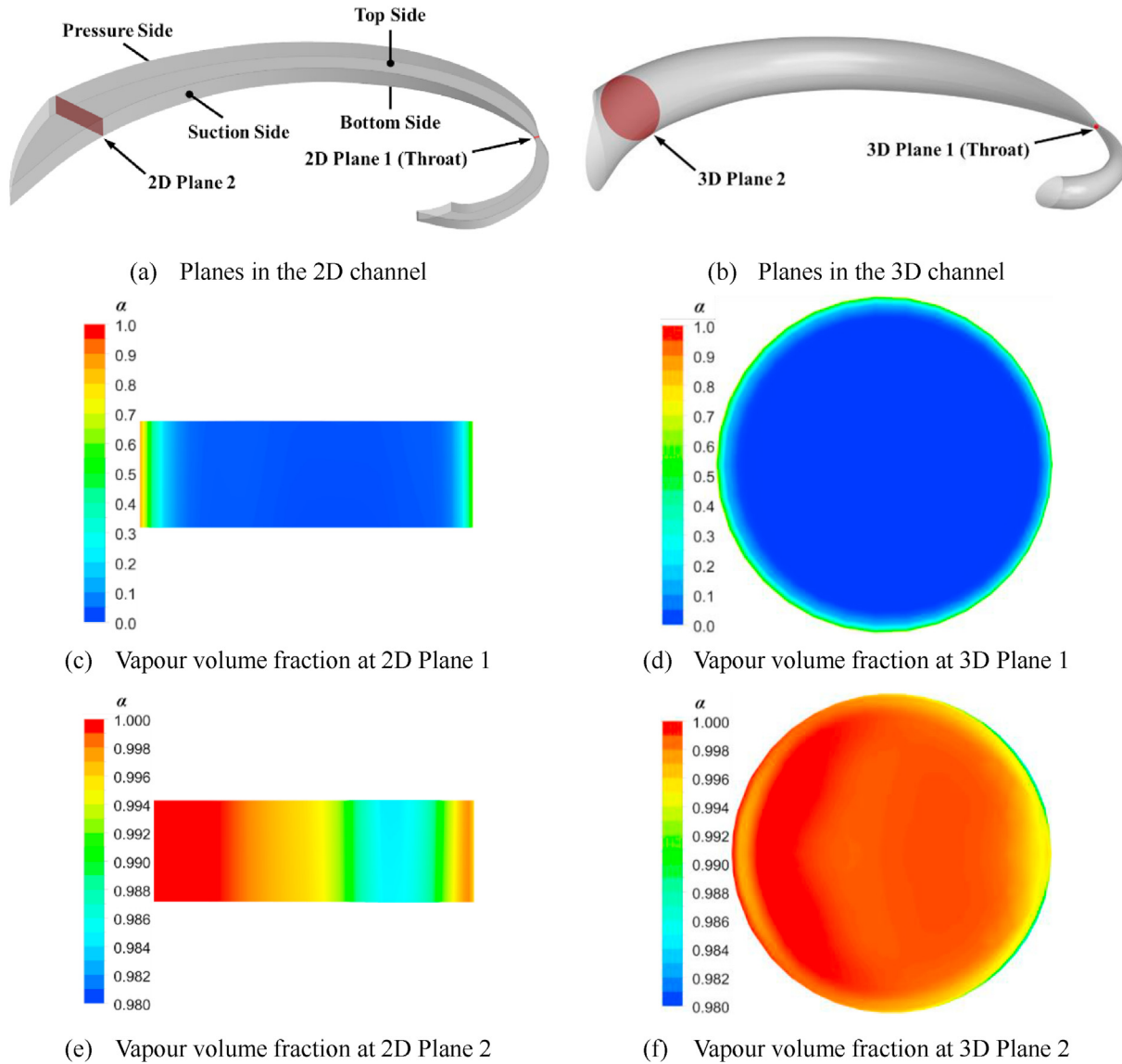


Fig. 18. Contours of the vapour volume fraction in cross-sections (c)-(f): Left side is the suction side and the right side is the pressure side.

section shown in Fig. 16(b), then reshaped from the 3D square to the 3D circle, as shown in Fig. 16(c).

To evaluate the shape factor, the pressure in the width direction is assumed to be approximately linear distributed, as shown in Fig. 16(a). Thus, the pressure on the pressure side and the suction side is $P + (\partial P / \partial r)Z/2$ and $P - (\partial P / \partial r)Z/2$, separately. The output power for the 3D square can be derived approximately as

$$P_{O_{\text{square}}}^{3D} = \frac{P_{O_{\text{rectangle}}}^{2D}}{\tau_Z} \quad (36)$$

For an element with the length δL and the 3D square cross-section, if the width of the element is far less than the radius of the center of the element, the torque on the pressure side and suction side caused by the pressure can be derived approximately as

$$\left(T_{O_{\text{square}}}^{3D}\right)^{PS+SS} = \left(\frac{\partial P}{\partial r}\right) Z^2 \delta L B_N \quad (37)$$

The torque on the top side and bottom side caused by the pressure can be derived approximately as

$$\left(T_{O_{\text{square}}}^{3D}\right)^{TS+BS} = PZ \frac{\partial Z}{\partial L} \delta L B_N \quad (38)$$

For an element with the length δL and the 3D circle cross-section, the torque on the pressure side and suction side caused by the pressure can be derived approximately as

$$\left(T_{O_{\text{circle}}}^{3D}\right)^{PS+SS} = \frac{\pi}{4} \left(\frac{\partial P}{\partial r}\right) Z^2 \delta L B_N \quad (39)$$

The torque on the top side and bottom side caused by the pressure can be derived approximately as

$$\left(T_{O_{\text{circle}}}^{3D}\right)^{TS+BS} = \frac{\pi}{4} PZ \frac{\partial Z}{\partial L} \delta L B_N \quad (40)$$

The relationship of the output power between the 3D square and the 3D circle can be derived as

Table 3
Performance of the impeller using 1D, 2D, and 3D methods under the design condition.

Parameters	1D	2D	3D
p^{in} (kPa)	1100	1100	1100
T^{in} (°C)	174	174	174
p^{out} (kPa)	101	101	101
m (kg/s)	5.00	6.31	5.22
N (rpm)	2200	2200	2200
α^{out}	0.992	0.990	0.988
X_g^{out}	0.070	0.080	0.081
W_l^{out} (m/s)	116.2	143.5	117.1
W_v^{out} (m/s)	118.7	133.1	125.2
To (N·m)	4.55	7.44	4.97
PO (kW)	10.5	17.2	11.5
PO_p^{PS+SS} (kW)	–	31.0	27.1
PO_p^{TS+SS} (kW)	30.4	32.2	31.5
PO_f^{PS+SS} (kW)	–	–1.2	–4.4
PO_p^{TS+BS} (kW)	–	11.0	9.2
PO_p^{TS+BS} (kW)	10.7	11.0	11.0
PO_f^{TS+BS} (kW)	–	0	–1.8
η (%)	7.20	11.82	7.90
CPU time (hours)	0.002	20	1500

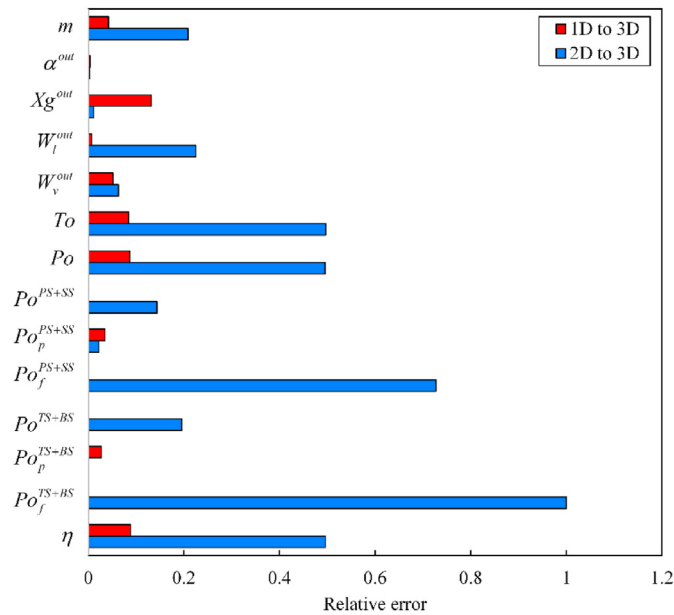


Fig. 19. Relative errors of performance parameters.

$$PO_{circle}^{3D} = \frac{\pi}{4} PO_{square}^{3D} \quad (41)$$

Thus, the shape factor is $\pi/4$.

The comparison between the experiment and the evaluated performance of the three models is illustrated in Fig. 17. Rane and He [33,54] suggested that proper bubble density number (5×10^7) and thermal phase changing model (Wolfert model [55]) through comparing Date's experimental results [32]. The mass flow rate obtained by the 1D model agrees with experimental results and the 3D model, but the mass flow rate obtained by the 2D model is much higher than other results. However, the output power obtained by the output power can agree with experimental results and the 3D model. The 1D model cannot be applied to the evaluation of the RMIT impeller's output power because the simple radial

equilibrium cannot be used to evaluate the pressure on the pressure line and suction line of the RMIT impeller. Therefore, the 1D model has benefit in reducing the CPU time and predicting the mass flow rate. Although there is large deviation of the mass flow rate between the 2D model and other models, the 2D model can predict the output power with the least deviation between the model and experimental results. Compared with the 3D model, the CPU hours cost by the 2D model is much less than the 3D model. Thus, the combination of the 1D model and the 2D model can be used for fast evaluation of the RMIT impeller's performance.

The disagreement of the mass flow rate between the 2D method and the 3D method can be attributed to the boundary effect near the top side and the bottom side. The cross-section of the 2D channel is rectangular as shown in Fig. 18(a), while the cross-section of the 3D channel is circular as shown in Fig. 18(b). Since there is only one layer in the z-direction and both the top side and the bottom side are symmetric boundaries, wall effects of the top side and the bottom side cannot be included in the 2D method. As shown in Fig. 18(c), the vapour is generated near the pressure side and the suction side. But in Fig. 18(d), there is a thin vapour ring generated on the wall. As shown in Fig. 18(f), there is liquid attached on the pressure side in the 3D method and there is also liquid tending to move towards the suction side. However, as shown in Fig. 18(e), wall effects of the top side and the bottom side cannot be evaluated in the 2D method. Thus, a much higher mass flow rate is derived in the 2D method than the 3D method.

4. Performance evaluation and flow details

4.1. Performance of the impeller at design condition

The total performance of the impeller under the design condition was evaluated by 1D, 2D and 3D methods and listed in Table 3. The consumed time of 1D is much less than 2D and 3D. The 3D method takes 75 times CPU hours of the 2D method and 750,000 times CPU hours of the 1D method. The huge reduction in the CPU time required shows the advantage of the 1D method. The turbine efficiency is defined by Equation (32).

Since the leakage loss and the frictional loss is significantly affected by the structure of the turbine and types of seals and bearings, the loss of the output power only contains the passage loss in the performance evaluation. However, it should be noted that the measured output power should be less than the output power evaluated in the paper, because the disk friction loss and the frictional losses caused by seals and bearings are not included in this paper. Reasonable evaluation methods of all friction losses for two-phase turbines need further investigation and validation. In this paper, the passage loss is the two-phase frictional pressure reduction for the 1D method, and it can be derived using the viscous stress of the fluid at the walls.

The loss of output power is evaluated using the two-phase frictional pressure reduction in the 1D method. For the 3D method, the total output power can be calculated by

$$PO = PO_p^{PS+SS} + PO_f^{PS+SS} + PO_p^{TS+BS} + PO_f^{TS+BS} + PO_p^{Outlet} \quad (42)$$

with

$$\begin{cases} PO_p = \iint P \vec{n} \cdot \vec{r} dA \\ PO_f = \iint \vec{F} \cdot \vec{v} dA - \iint P \vec{n} \cdot \vec{r} dA \end{cases} \quad (43)$$

The relative errors of 1D or 2D performance parameters compared with 3D in Table 3 are illustrated in Fig. 19. The relative error of the mass flow rate between 1D result and the 3D result is

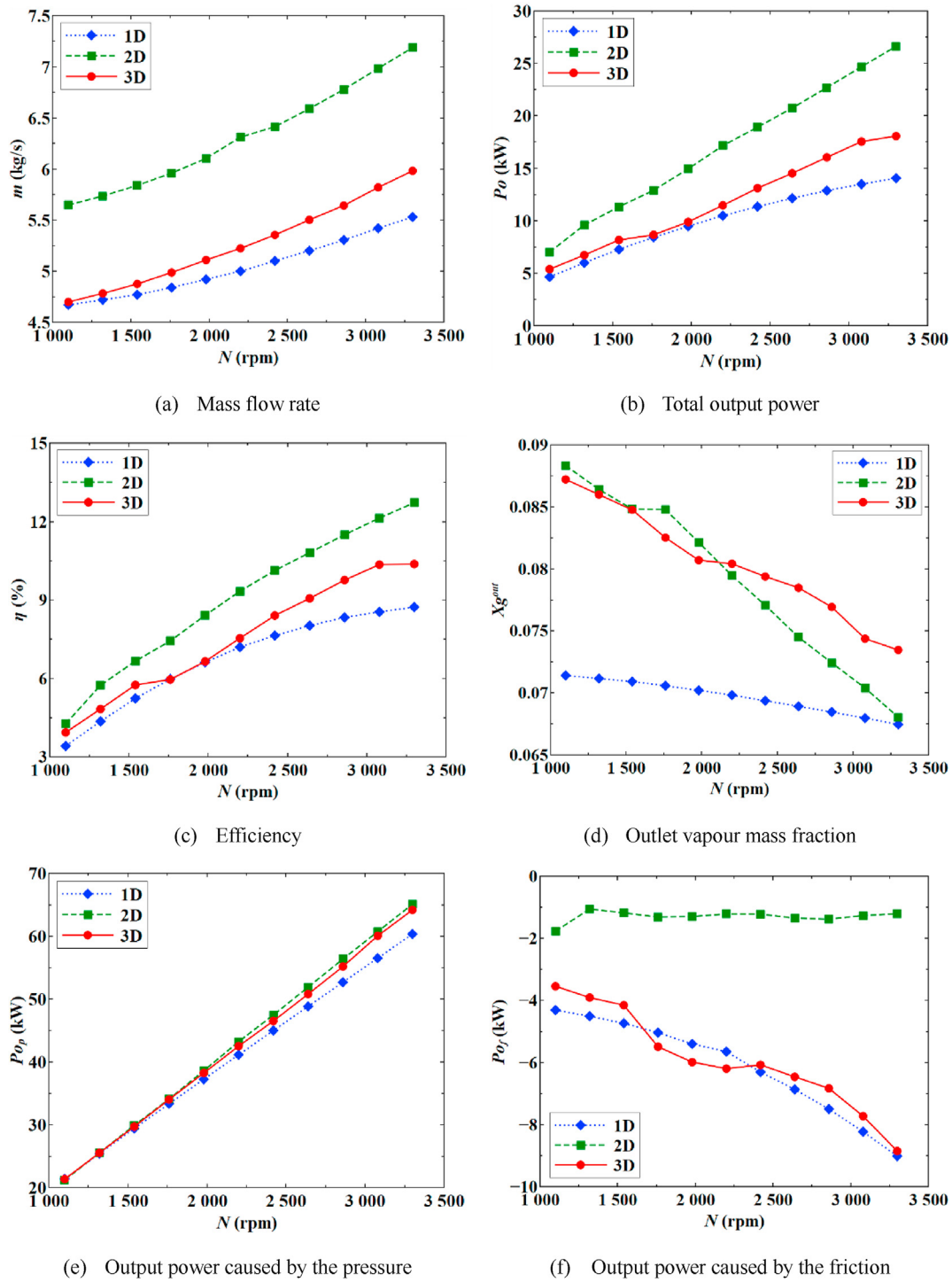


Fig. 20. Performance parameters under various rotational speeds.

4.2%, but 2D to 3D error is 20.9%. Because in the 2D method boundary conditions on the top side and the bottom side are symmetrical surfaces, the mass flow rate deduction caused by the viscous effect on the top side and the bottom side is not included, and the 2D method predicts a higher mass flow rate than 1D and 3D methods. For the same reason, the 2D method leads to faster relative velocities than 1D and 3D methods. The 2D method also predicts a higher total output power, because 2D cannot take the

frictional power on the top side and the bottom side into account. However, the 2D method has a benefit in predicting the output power caused by the pressure P_{o_p} across the walls of the channel, because it can include nonuniform effects in the circumferential direction. The relative error of the 2D method in the power is 2.2%. The ability to predict circumferential flow shows that the 2D method can be implemented into the 1D method to reduce the time required by the 3D method.

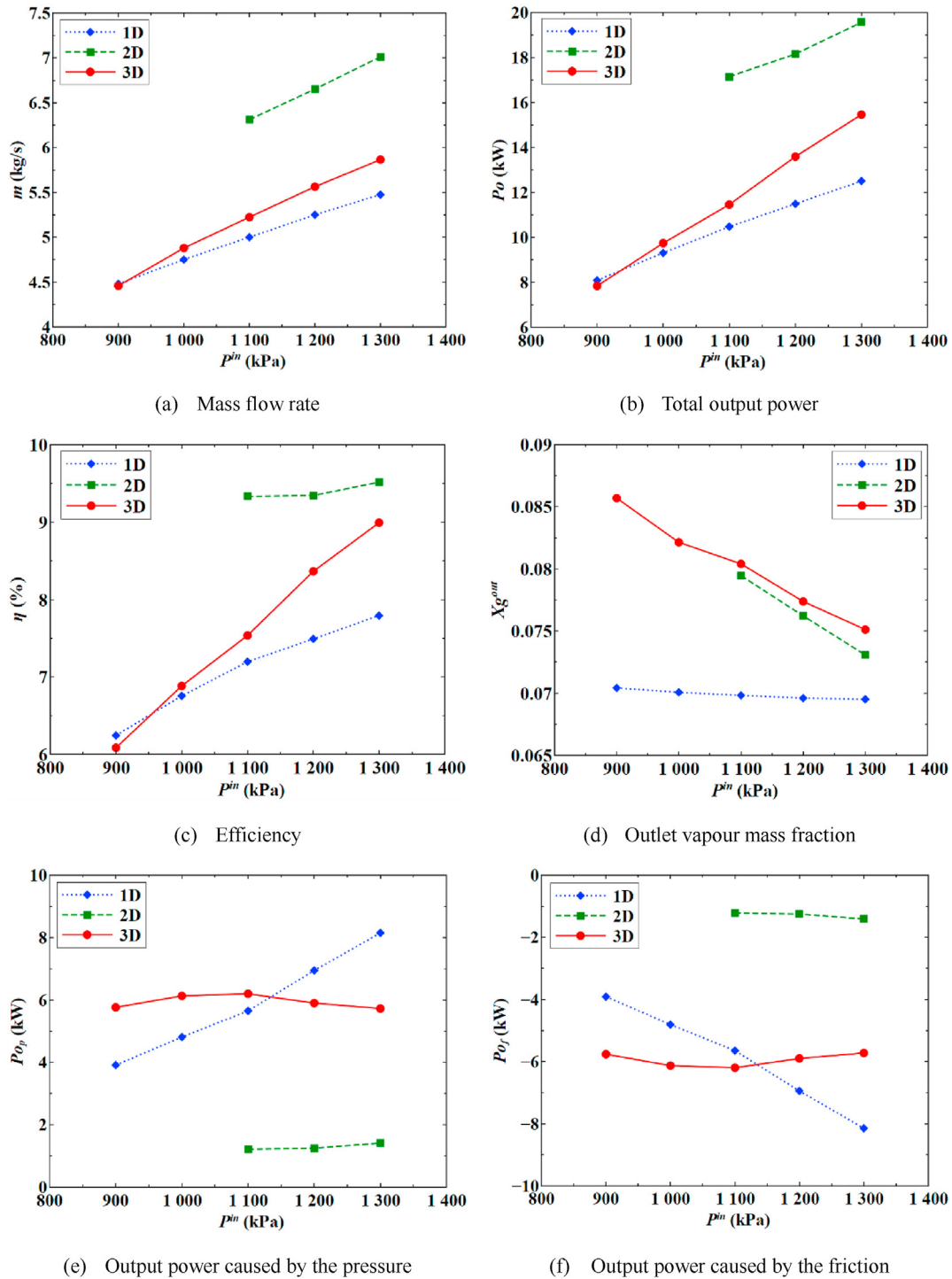


Fig. 21. Performance parameters under inlet pressure.

4.2. Influences of various factors

4.2.1. Rotational speed

In combined geothermal systems, the mass flow rate may have to be changed according to requirements from the integrated system and geological environments. An easy way to vary the mass flow rate of the two-phase turbine is to change the rotational speed of the two-phase turbine. The performance of the turbine under various rotational speed is important for optimizing system

parameters of the trilateral flash geothermal system or other integrated geothermal systems.

The performance of the impeller under various rotational speeds is shown in Fig. 20. The inlet pressure P^{in} , inlet temperature T^{in} and outlet pressure P^{out} are the same as those under the design working condition. As shown in Fig. 20(a), the mass flow rate m increases with the rotational speed N . The 1D method underestimates the flow rate compared with the 3D method. The deviation between 1D and 3D increases with N . The 2D method

overpredicts m because the 2D method cannot include the viscous effect on the top side and the bottom side. Compared with the 3D method, the deviation between 2D and 3D is constant.

As illustrated in Fig. 20(b), the output power P_o increases with rotational speed. P_o derived from the 1D method is lower than the 3D method. There is a certain deviation between the 1D method and the 3D method which is caused by the empirical correlation of the two-phase frictional pressure reduction. The deviation reaches the lowest at 80% of the design rotational speed and increases with

the rotational speed from 1760 rpm to 3080 rpm. The 2D method overpredicts P_o compared with the 3D method. The deviation between 2D and 3D increases remarkably with N .

The turbine efficiency η is defined by Equation (32) and increases with N as shown in Fig. 20(c). The turbine efficiency calculated by the 1D method is the lowest among the three methods. The deviation between the 1D and 3D method reaches the lowest at 1760 rpm.

The outlet vapour mass fraction Xg^{out} is averaged on the outlet

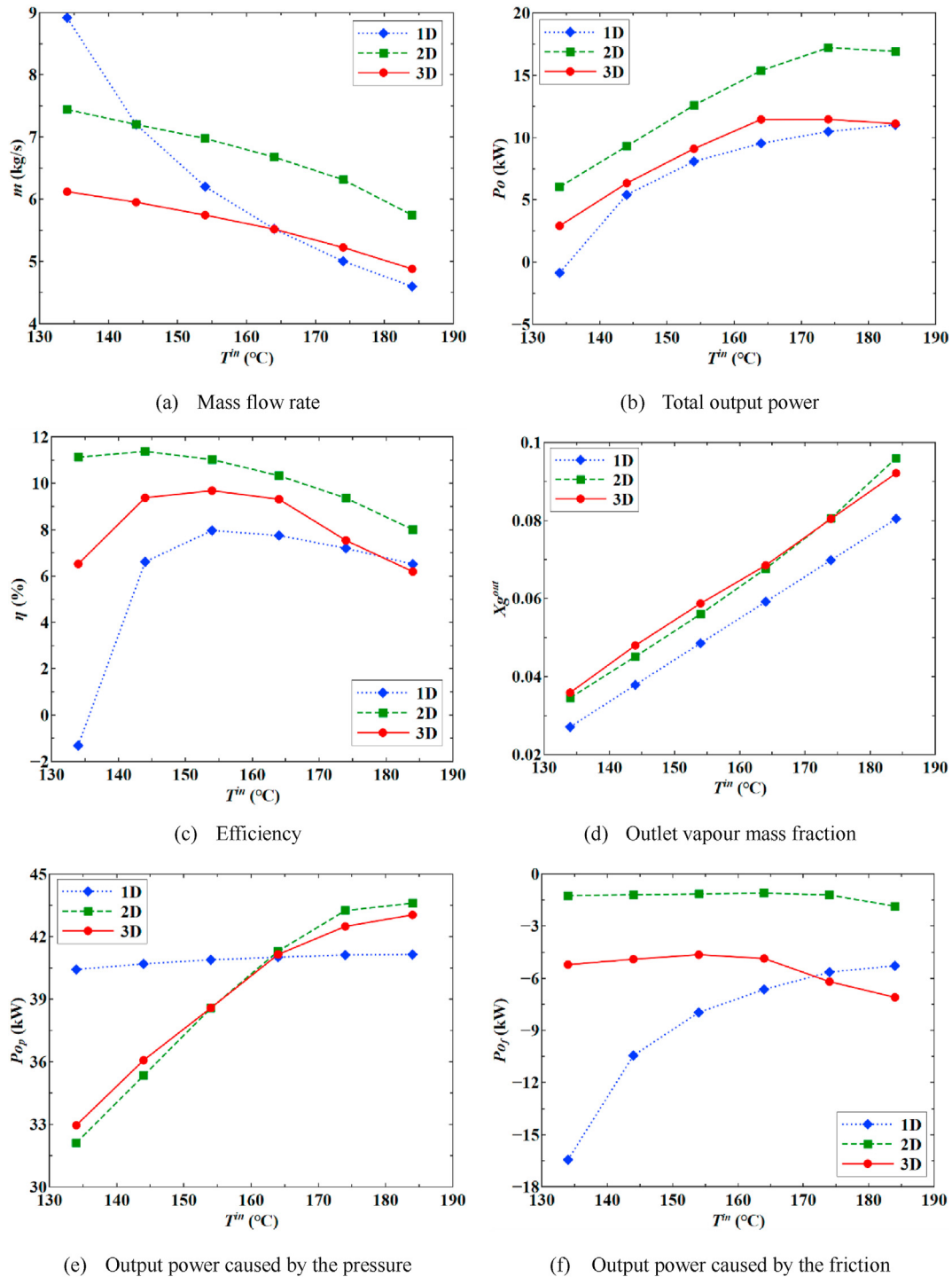


Fig. 22. Performance parameters under various working conditions under various inlet temperatures.

boundary using the mass flow rate and decreases with N , as illustrated in Fig. 20(d). The 1D method underestimates Xg^{out} ranging from 0.067 to 0.071. Xg^{out} derived by the 2D method agrees with the 3D method. The deviation between 2D and 3D is the lowest at 1540 rpm.

As shown in Fig. 20(e), the output power caused by the pressure Po_p is consistent among the three methods, while there is a certain deviation between 1D and 3D, and the deviation increases with flow rate. Since the 2D method cannot include the viscous effect on the top side and the bottom side, the output power caused by the friction Po_f is much higher than 3D. Po_f predicted by the 1D method agrees with the 3D method, as illustrated in Fig. 20(f).

4.2.2. Inlet pressure

The wellhead pressure can also vary with time due to geological factors in enhanced geothermal systems. The wellhead pressure is almost equal to the inlet pressure of the turbine if the pressure reduction in pipes and heat exchangers is neglected. The inlet pressure of the impeller affects thermophysical properties, the pressure difference between the inlet and outlet of the impeller, subcooling degree at the inlet, and so on. If the outlet boundary condition is fixed to the design condition and the inlet temperature is the design temperature, the performance of the impeller is varied with the inlet pressure as illustrated in Fig. 21.

As shown in Fig. 21(a), m increases with P^{in} , the 1D method underpredicts m if P^{in} is higher than 900 kPa, and the deviation between 1D and 3D method increases with P^{in} . When P^{in} is 900 kPa, the deviation is 0.5%; when P^{in} is 1300 kPa, the deviation is 6.7%. The 2D method overestimates m and the deviation between the 2D method and the 3D method is about 20%. The 2D method has a limitation on the predictions under various inlet pressures, since it has convergence problems if the inlet pressure P^{in} is less than 1100 kPa. There is strong non-physical phenomenon (for example, extremely high Mach number) and unsteady flow (such as bubble breakage and droplets coalescence) near the throat of the channel in the 2D simulation. As P^{in} decreases, the subcooling degree of the fluid is reduced and the vaporization near the throat becomes more dramatic. Due to lacking the wall effects of the top side and the bottom side, the 2D method overestimates the mass flow rate and the velocity inside the channel. Therefore, extreme high relative velocity is predicted in the 2D simulation, and the phase-changing process near the throat is affected significantly by the high velocity. The result is that the 2D method cannot get converged if P^{in} is lower than 1100 kPa.

In Fig. 21(b), Po increases with P^{in} , the 1D method underpredicts Po if P^{in} is higher than 900 kPa, and the deviation between 1D and 3D method increases with P^{in} . The 2D method overestimates Po with over 20% deviation.

In Fig. 21(c), the turbine efficiency η increases with P^{in} and the

1D method can predict η with less than 2% deviation. In Fig. 21(d), Xg^{out} decreases with P^{in} because the subcooling degree at the inlet increases with P^{in} . The 1D method underpredicts Xg^{out} compared with the 3D method. The 2D method can predict Xg^{out} with less than 2.7% deviation.

As shown in Fig. 21(e), Po_p agrees with each other among the three methods, although there is a certain deviation between 1D and 3D. Po_f obtained by 3D method is almost constant and varies between -5.7 kW and -6.2 kW. The deviation between 1D and 3D method reaches the lowest when P^{in} is 1100 kPa. The 2D method underpredicts Po_f and varies between -1.2 kW and -1.4 kW as shown in Fig. 21(f).

4.2.3. Inlet temperature

The inlet temperature of the impeller determines the subcooling degree of the inflow liquid. The saturation temperature for the inflow at the inlet pressure is 184 °C. Under the design condition, the subcooling degree is 10 °C which can ensure that there is no flashing at the entrance to the channel. During the start/end phase in the real operation, the inlet temperature may vary with time. In addition, the wellhead temperature may also vary with season or year. The performance of the turbine may be significantly influenced by the varying temperature. The flashing inception point is also varied with the inlet temperature. Fig. 22 illustrates the relationship between the inlet temperature and the performance of the impeller at the design inlet pressure and the design outlet pressure. The range of the inlet temperature is between 134 °C and 184 °C.

In Fig. 22(a), the mass flow rate m decreases as the inlet temperature T^{in} increases. In other words, m increases with inlet subcooling degree. The 2D method overestimates m over the entire range of T^{in} . If T^{in} is lower than 174 °C, the 1D method overestimates m . If T^{in} is higher than 174 °C, the 1D method underpredicts m .

In Fig. 22(b), Po obtained by the 3D method increases with T^{in} if T^{in} is lower than 164 °C. The 2D method overestimates Po , and the 1D method underpredicts Po . If T^{in} varies between 144 °C and 184 °C, the deviation between the 1D method and the 3D method is lower than that between the 2D method and the 3D method.

In Fig. 22(c), the maximum turbine efficiency η obtained by the 3D method is 9.7% when T^{in} is 154 °C, and the 2D method overestimates η . If T^{in} is lower than 174 °C, the 1D method underpredicts η . The deviation of the 1D method reaches the lowest when T^{in} varies between 174 °C and 184 °C. In Fig. 22(d), Xg^{out} increases with T^{in} and the deviation between the 2D method and the 3D method is lower than that between the 1D method and the 3D method. At 174 °C, the deviation of the 2D method reaches the lowest value.

In Fig. 22(e), Po_p obtained by the 2D method agrees with the 3D method, but the 1D method derives almost constant Po_p at various T^{in} . In Fig. 22(f), the 2D method underpredicts Po_f and the 1D method overestimates Po_f if T_{in} is lower than 174 °C. Po_p is

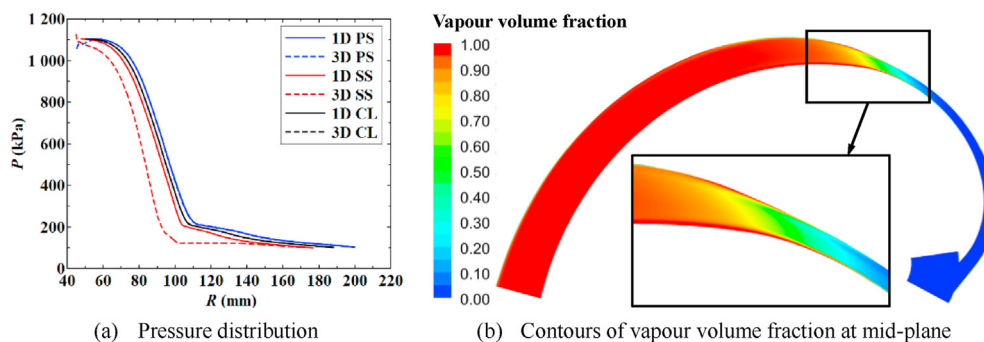


Fig. 23. The pressure distribution and contours of vapour volume fraction at 184 °C.

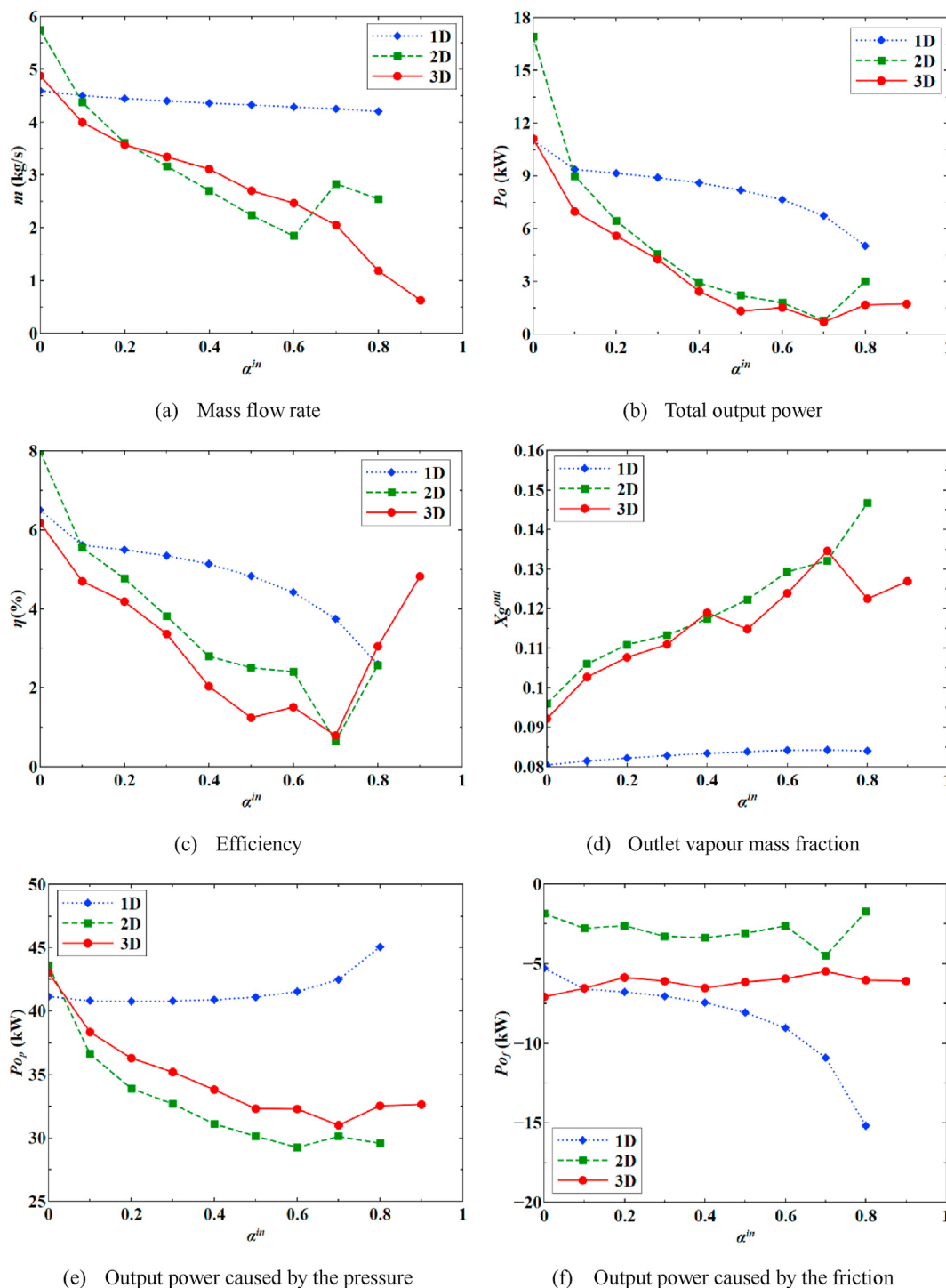


Fig. 24. Performance parameters under various working conditions under various inlet volume fractions.

Table 4
Boundary conditions for the two-phase reaction turbine in Section 4.2.1 and 4.2.2

Sections	Fixed boundaries	Variable boundary
Section 4.2.1	Design inlet pressure, design inlet temperature, design inlet vapour volume fraction, design outlet pressure	Rotational speed
Section 4.2.2	Design inlet temperature, design inlet vapour volume fraction, design outlet pressure, design rotational speed	Inlet pressure

determined by the distribution of the pressure and the geometry of the pressure side and suction side. The pressure distribution on the pressure side and the suction side obtained by the 1D method is

derived by the pressure gradient on the normal direction. The significant variation of the output power in Fig. 22(e) obtained by the 2D/3D method is caused by the non-equilibrium effect on the

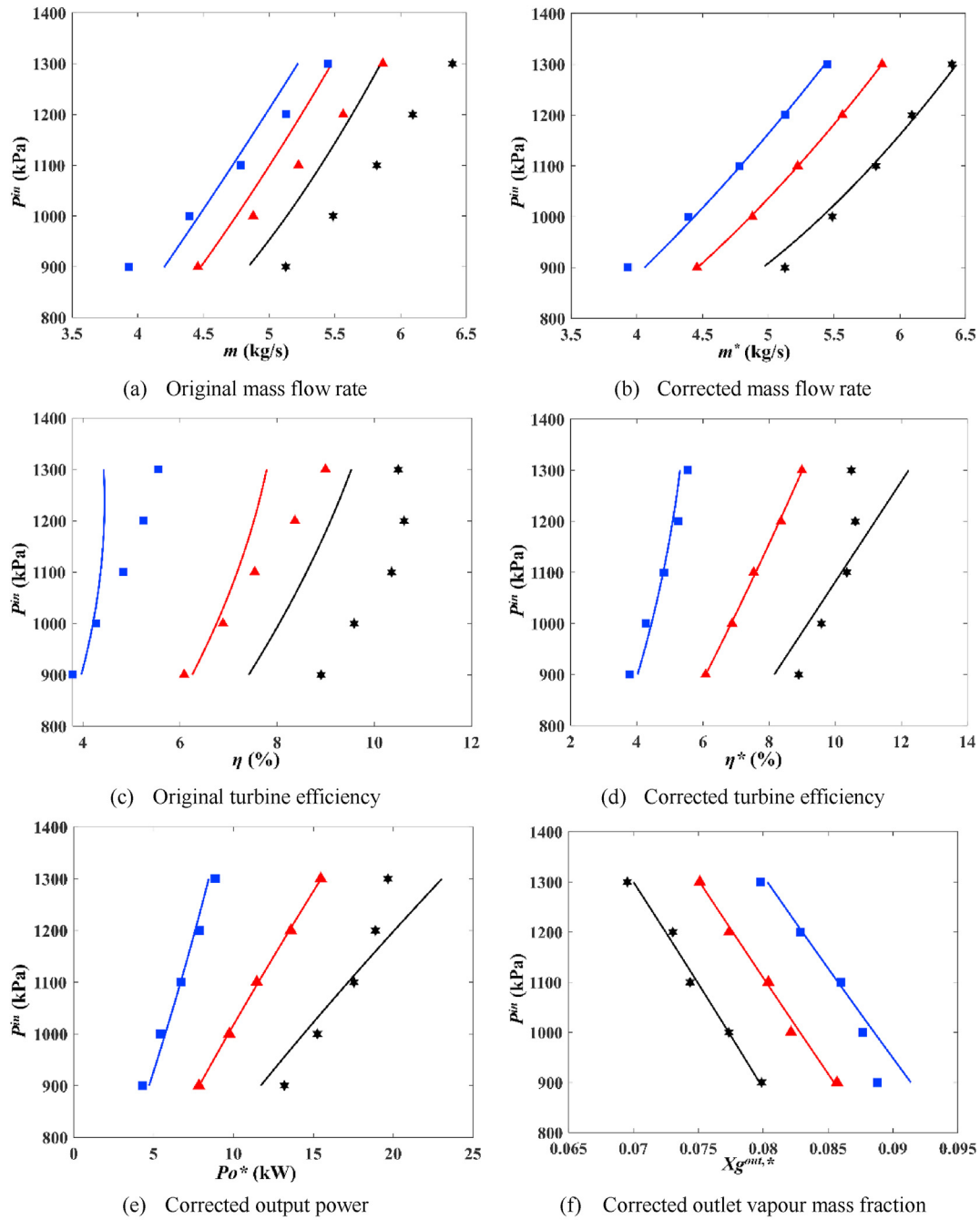


Fig. 25. Original and corrected performance using the 1D method compared with the 3D method.

rotation direction. As illustrated in Fig. 23(a), the pressure distribution on the suction side obtained by the 1D method deviates from the pressure obtained by the 1D method while the pressure on the pressure side and the averaged pressure on cross-sections obtained by the 3D method agree with the 1D method. Because the pressure on the suction side obtained by the 1D method is derived using the simple radial equilibrium equation, it indicates that there are strong non-equilibrium effects near the suction side. As shown in Fig. 23(b), the flashing inception point on the suction side is in front of the inception point on the pressure side, and the vapour layer is much longer on the suction side than the pressure side. Therefore, due to the non-equilibrium effect of the nucleation, the pressure on the suction side obtained by the 2D/3D method is

much lower than that obtained by the 1D method, and Po_p obtained by the 2D/3D method deviates from the 1D method as shown in Fig. 22(e).

4.2.4. Inlet vapour volume fraction

The outflow from the wellhead may be subcooled liquid, overheated vapour, and liquid-vapour mixture. If the two-mixture drives the turbine directly, the influence of the inlet vapour volume fraction on the performance of the turbine is shown in Fig. 24. All other boundary conditions are the same with design parameters except the inlet temperature and the inlet vapour volume fraction. The inlet temperature is the saturation temperature. Both the 1D and the 2D method cannot get converged when the inlet vapour

volume fraction is higher than 0.8.

In Fig. 24(a), m obtained by the 3D method decreases as α^{in} increases. But the 1D method predicts almost constant value, and the deviation between the 1D method and the 3D method increases with α^{in} . The 2D method agrees with the 3D method if α^{in} is lower than 0.6. In Fig. 24(b), P_o decreases as α^{in} increases if α^{in} is lower than 0.5. The 2D method agrees with the 3D method if α^{in} is higher than 0.1. The 1D method overestimates the output power.

In Fig. 24(c), the turbine efficiency η obtained by the 3D method decreases as α^{in} increases if α^{in} is lower than 0.5. When α^{in} is higher than 0.7, η increases with α^{in} significantly. The 2D method agrees with the 3D method if α^{in} is higher than 0.1. In Fig. 24(d), Xg^{out} obtained by the 3D method increases with α^{in} if α^{in} is lower than 0.4. The 1D method underpredicts Xg^{out} , but the 2D method agrees with the 3D method if α^{in} is lower than 0.7.

As shown in Fig. 24(e), P_o_p obtained by the 3D method decreases as α^{in} increases if α^{in} is lower than 0.7. The 1D method overestimates P_o_p , but the 2D method agrees with the 3D method. In Fig. 24(f), P_o_f obtained by the 3D method varies between -5.5 kW and -7.1 kW. The 2D method underpredicts P_o_f , and the 1D method agrees with the 3D method if α^{in} is lower than 0.4.

4.3. Integration with the geothermal system

4.3.1. Performance map

The performance of the impeller has been evaluated under various inlet pressures or rotational speeds in previous sections, and the 1D method agrees well with the 3D method. Boundary conditions at various rotational speeds and inlet pressures are listed in Table 4. It can be found that those working conditions are not sufficient to generate the performance map, which represents the performance of the impeller if both the inlet pressure and the rotational speed are changed. Using the 3D method, the performance map of the impeller can be evaluated certainly, but it will cost a mass of computational resources. Using the 1D method can reduce the requirement of computational effort. However, there is a certain deviation between 1D and 3D method, which increases with the rotational speed and the inlet pressure in previous sections.

Fig. 25(a) shows the performance map using the 1D method and the deviation between 1D and 3D method under several selected

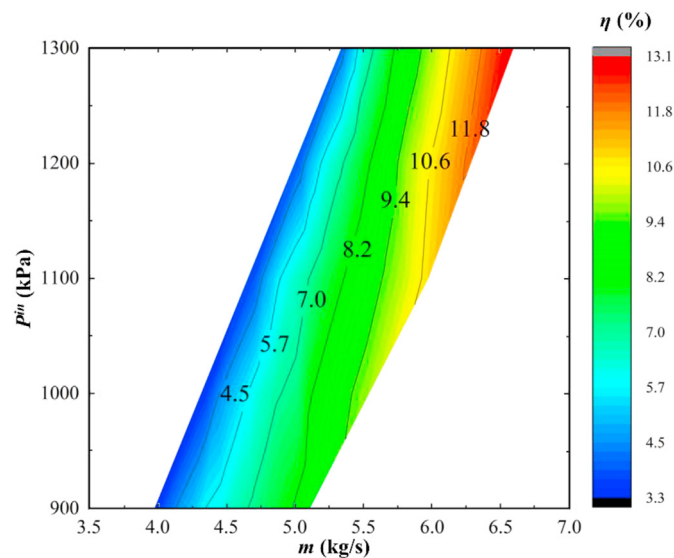


Fig. 26. The performance map of the impeller.

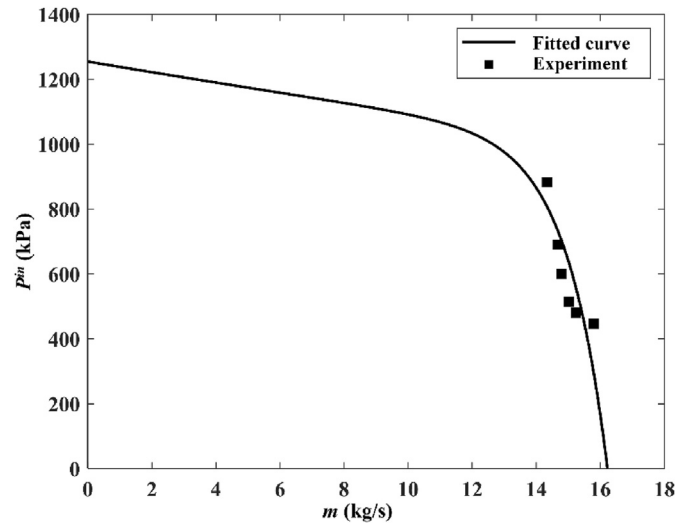
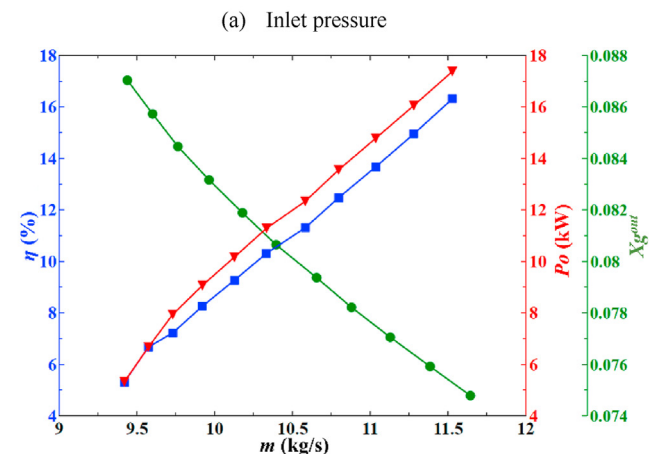
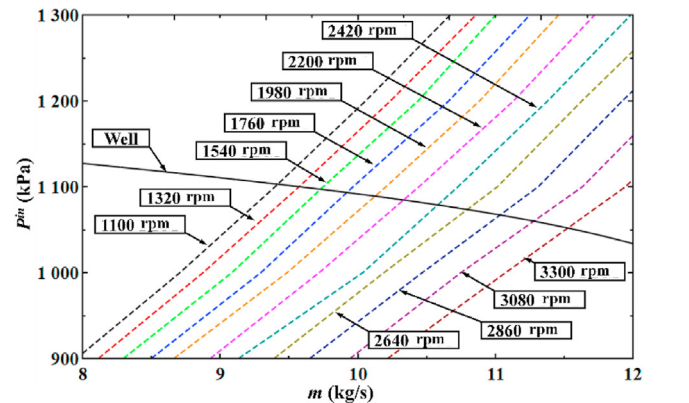


Fig. 27. Mass flow rate of 'LA-8' under various inlet pressures [44,67].

working conditions. The deviation of the mass flow rate can be evaluated using Equation (44).

$$\epsilon_m(N, P) = \frac{m_{3D}(N, P) - m_{1D}(N, P)}{m_{1D}(N, P)} \quad (44)$$

If the deviation has been already known, the corrected 1D mass



(b) Efficiency, output power and outlet vapour mass fraction

Fig. 28. Performance of the turbine under the wellhead condition.

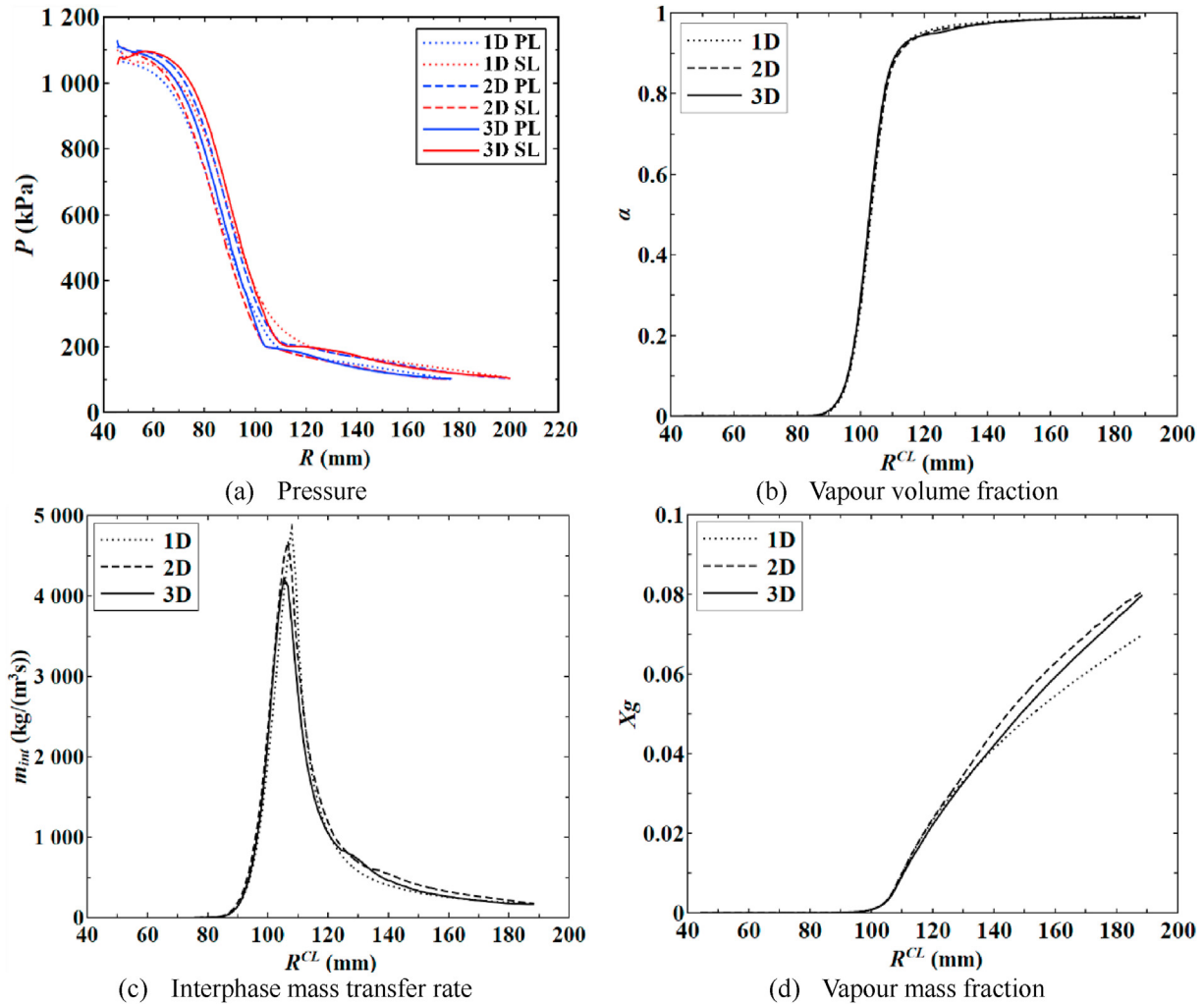


Fig. 29. Distribution of the pressure and the vapour volume fraction.

flow rate can be derived as

$$m_{1D}^*(N, P) = [1 + \epsilon_m(N, P)]m_{1D}(N, P) \quad (45)$$

Using the data in Figs. 13 and 14, the deviation of the mass flow rate can be fitted using the following equation

$$\epsilon_m^*(N, P) = \lambda_{m1}N^2 + \lambda_{m2}N + \lambda_{m3}P^2 + \lambda_{m4}P + \lambda_{m5} \quad (46)$$

with $\lambda_{m1} = -1.047 \times 10^{-9}$, $\lambda_{m2} = 3.813 \times 10^{-5}$, $\lambda_{m3} = -2.752 \times 10^{-7}$, $\lambda_{m4} = 7.907 \times 10^{-4}$ and $\lambda_{m5} = -0.5711$.

The corrected 1D mass flow rate can be evaluated using Equation (45) if the deviation is replaced with Equation (46). As shown in Fig. 25(b), the deviation of the mass flow rate has been largely reduced.

The same method can also be applied to fit the deviation of the turbine efficiency and Equation (47) can be derived

$$\epsilon_\eta^*(N, P) = \lambda_{\eta1}N^2 + \lambda_{\eta2}N + \lambda_{\eta3}P^2 + \lambda_{\eta4}P + \lambda_{\eta5} \quad (47)$$

with $\lambda_{\eta1} = 1.077 \times 10^{-7}$, $\lambda_{\eta2} = -4.255 \times 10^{-4}$, $\lambda_{\eta3} = 1.793 \times 10^{-7}$, $\lambda_{\eta4} = 6.197 \times 10^{-5}$ and $\lambda_{\eta5} = 0.1886$. The turbine efficiency is defined by Equation (32).

The deviation of the turbine efficiency is shown in Fig. 25(c) and (d). The deviation has also been reduced remarkably when the

rotational speed is 1320 rpm and 2200 rpm. But there is still a certain deviation when the rotational speed is 3080 rpm, and the inlet pressure is 1300 kPa.

The output power can be corrected by making use of the corrected mass flow rate and the turbine efficiency using Equation (48). The corrected output power is illustrated in Fig. 25(e).

$$Po^* = \Delta H_s m^* \eta^* \quad (48)$$

The outlet vapour mass fraction can also be corrected using the same method as the corrected mass flow. The deviation of the outlet vapour mass fraction between 1D and 3D method is fitted using Equation (49). The corrected outlet vapour mass fraction is illustrated in Fig. 25(f).

$$\epsilon_x^*(N, P) = \lambda_{x1}N^2 + \lambda_{x2}N + \lambda_{x3}P^2 + \lambda_{x4}P + \lambda_{x5} \quad (49)$$

with $\lambda_{x1} = 5.911 \times 10^{-9}$, $\lambda_{x2} = -8.381 \times 10^{-5}$, $\lambda_{x3} = -5.804 \times 10^{-8}$, $\lambda_{x4} = -2.055 \times 10^{-4}$ and $\lambda_{x5} = 0.6104$.

Using the above-corrected mass flow rate and the corrected turbine efficiency, the performance map can be derived as shown in Fig. 26. The turbine efficiency increases with mass flow and inlet pressure. It should be noted that the high mass flow rate should be achieved under high rotational speed.

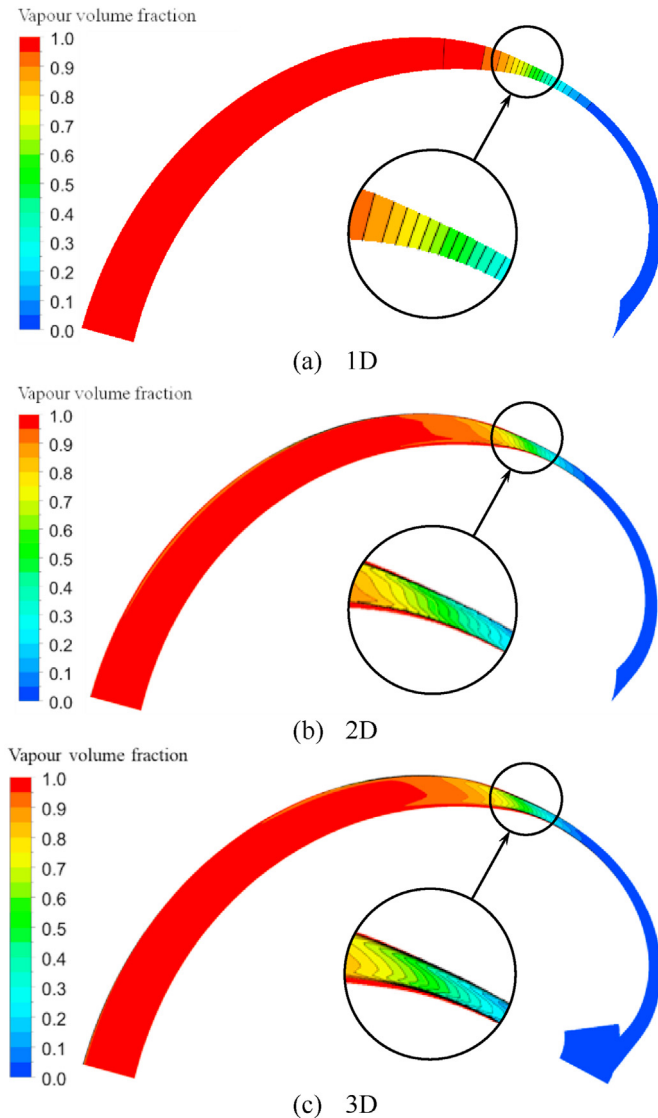


Fig. 30. Contours of vapour volume fraction in the plane $z = 0$ mm.

4.3.2. Influence of system parameters on the two-phase reaction turbine

Operation parameters of the geothermal system affects considerably the performance of the turbine. The mass flow rate of ‘LA-8’ [44,67] under various inlet pressure is illustrated in Fig. 27.

The relationship between the inlet pressure and the mass flow rate can be fitted using Equation (50).

$$P = \zeta_1 e^{\zeta_2 m} + \zeta_3 e^{\zeta_4 m} \quad (50)$$

with $\zeta_1 = -0.003031$, $\zeta_2 = 0.7839$, $\zeta_3 = 1255$ and $\zeta_4 = -0.01324$.

Two impellers are used in a two-phase turbine to match the requirement of the mass flow rate. A series of points can be derived if the curve of ‘LA-8’ and the performance map is drawn in a common figure, as shown in Fig. 28(a). Intersection points are working conditions for various rotational speeds. The inlet pressure increases as the rotational speed decreases. The mass flow rate decreases with rotational speed. As shown in Fig. 28(b), the turbine efficiency under these working conditions increases from 5.3% to 16.3% with mass flow rate as well as the rotational speed. The

output power increases from 10.6 kW to 34.8 kW with the mass flow rate. However, the outlet vapour mass fraction decreases from 0.082 to 0.075. The reduction of the vapour at the outlet decreases the production of the freshwater. Therefore, there should be a balance between the output power and the quantity of the freshwater.

For a given inlet pressure, the performance of the turbine can also be varied using different subcooling degrees at the inlet of the turbine. When the inlet temperature of the turbine decreases, the subcooling degree increases, the mass flow rate increases, the turbine efficiency increases if the inlet temperature is higher than 154 °C, the output power decreases if the inlet temperature is lower than 164 °C, and the outlet vapour mass fraction decreases as shown in Fig. 22. For the given inlet pressure, if the mass flow rate is higher than the required value by the system, the rotational speed of the turbine should be decreased as illustrated in Fig. 28(a), the turbine efficiency and the output power decrease, and the outlet vapour mass fraction increases as shown in Fig. 20(b). In conclusion, the increases of the subcooling degree cause a reduction in the turbine efficiency, output power and rotational speed.

The increases of the inlet subcooling degree cause a reduction in the outlet vapour mass fraction, while the reduction of the rotational speed may increase of the outlet vapour mass fraction. There is no benefit in terms of the turbine efficiency, the output power and the production of the freshwater if the subcooling degree increases. But it should be noted that the reduction of the turbine efficiency and the output power is almost constant if the subcooling degrees is varied within 20 °C as shown in Fig. 22. In terms of the design and operation, a certain subcooling degree brings benefits. For example, if the saturation liquid flows into the turbine, the flashing may be triggered by the geometry of the inlet section and not controlled by the cross-sectional area of the channel. The subcooling liquid at the inlet section of the channel will make the design process much simpler than the saturation liquid. Meanwhile, the flashing triggered by the geometry of the inlet section may be highly unsteady and induces severe vibration to the shaft. Therefore, a certain subcooling degree is beneficial to the design and the operation of the turbine.

The inflow of the turbine may also be the two-phase mixture. As shown in Fig. 24, the increase of the inlet vapour volume fraction brings the reduction of the mass flow rate and the output power if the inlet vapour volume fraction is lower than 0.5. If the vapour volume fraction of the outflow from the well head increases and the mass flow rate remains constant, the rotational speed increases, the turbine efficiency increases and the outlet vapour mass fraction increases. The reduction of the flow rate may be beyond the ability to adjust rotational speed.

4.4. Flow details in the channel

4.4.1. Distribution of averaged flow parameters

The three models can be further compared on flow details in the channel. The distribution of flow parameters can reflect the average flow in the channel. The pressure in Fig. 29(a) is along the pressure line and suction line which are intersection curves between the pressure side/suction side and the plane $z = 0$. The pressure distribution of 2D simulation agrees well with the 3D simulation, so Po_p in 2D is consistent with 3D results. There is sharp turning in 2D and 3D distribution, but the pressure decreases gradually in 1D results. The disagreement near the entrance of the channel between 1D and 2D/3D is caused by the incidence of the inflow. The distribution of the vapour volume fraction is along the center line of the channel as shown in Fig. 29(b). Good agreement throughout the channel indicates that 1D vapour volume fraction can represent the averaged distribution in 2D and 3D channels, although the phase-

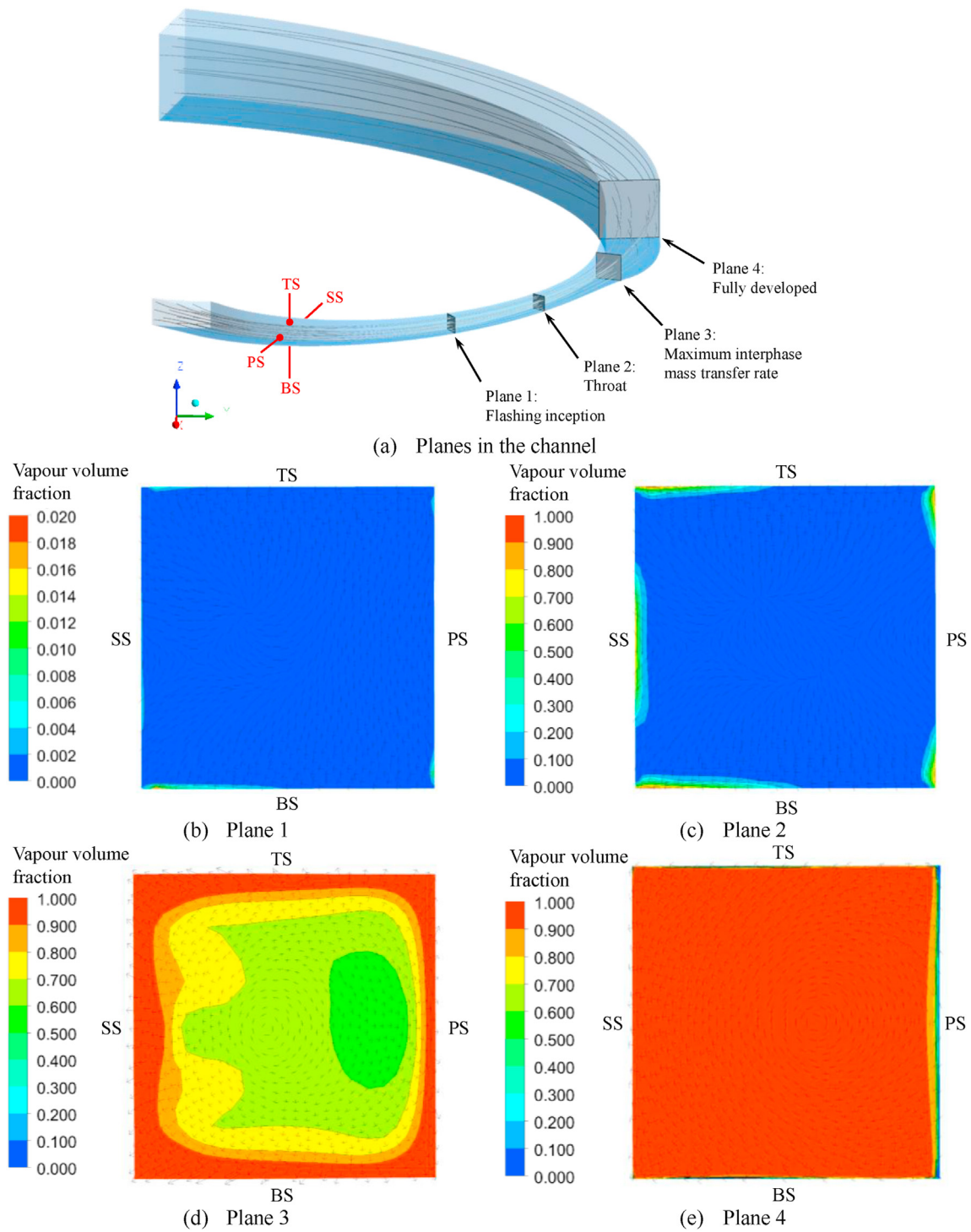


Fig. 31. Contours of vapour volume fraction and vectors of the mixture velocity
 The mixture velocity is defined by $W_m = (1 - X_g)W_l + X_gW_v$

changing in 2D and 3D is non-equilibrium. As shown in Fig. 29(c), the peak interphase mass transfer rate is 4120 kg/m³s for 3D at $R_{cl} = 106.7$ mm, while the 1D peak value is higher than the 3D value. The position of the peak value is at the downstream of the throat. The vapour mass fraction shows certain disagreement after the peak value of the interphase mass transfer rate as illustrated in Fig. 29(d).

4.4.2. Three-dimensional internal flow

The internal flow in the rotational channel is three dimensional and related to Rossby number and Eckman number, which is explained by Greitzer et al. [68]. However, in the 1D method, the flow is assumed to be uniform in cross-sections of the channel, and the flow is only along the center line. In the 2D method, the flow has the circumferential component and the component along the center line. In the 3D method, the flow has the spanwise component besides the other two components. Although the distribution of the averaged vapour volume fraction agrees well among the three methods, there is significant non-homogenous flashing phenomenon in the channel as shown in Fig. 30. In the 1D result, the vapour increases gradually near the throat of the channel, and the contours are normal to the flow direction, as illustrated in Fig. 30(a). In the 3D result, the vapour is generated from the walls of the channel into the center, as shown in Fig. 30(c). It also indicates that the liquid tends to concentrate near the pressure side due to the centrifugal force since the vapour volume fraction near the pressure side is much lower than the suction side near the throat. Since the 2D result has good agreement with the 3D result, it can be concluded that the 2D method can illustrate the attachment of the liquid which cannot be predicted by the 1D method as illustrated in Fig. 30(b).

Four cross-sections are cut inside the channel as shown in Fig. 31(a). The flashing starts near $R_{cl} = 83.0$ mm (Plane 1), which is at the upstream of the throat (Plane 2). The maximum interphase mass transfer rate in Fig. 29(c) locates at Plane 3. After Plane 4, the flashing process has been fully developed, since the vapour volume fraction is over 0.986. In Fig. 31(b), the flashing starts near the corners of the four walls. Relative velocity vectors illustrate that there is recirculation in the spanwise direction. In Fig. 31(c), the flashing has been further developed near the walls. In Fig. 31(d), the vapour has fully covered all walls and the flashing develops from walls into the middle of the channel. In Fig. 31(e), there is liquid attached on the pressure side due to the centrifugal force, although the flashing has been fully developed.

The accuracy, applicability, and computational time of the three methods are summarized in Table 5. The 1D method can predict the mass flow rate and output power rapidly, and it can obtain accurate performance results under various rotational speeds and inlet pressures. The 2D method can derive the outlet vapour mass fraction and the output power caused by the pressure with high

accuracy in a medium computational time, and it can reflect the non-uniform flow in the direction of rotation. However, the 2D method overestimates the flow rate and cannot reflect the wall effects of the top side and the bottom side. Although the 3D method can obtain the detailed flow field, it takes a lot of computational time.

5. Conclusion

The paper presents three performance evaluation methods and are applied to the two-phase reaction turbine for total flow geothermal systems under various working conditions. Influences of various operating factors of the system on the performance are examined and the flow details in the impeller channels are clarified. The following conclusions are made:

- (1) The 1D, 2D and 3D methods and the algorithm for the 1D method are proposed based on conservation equations and closure models of the two-phase flow. The three methods are validated with the experimental results at various rotational speeds. The 1D method takes less than 15 CPU minutes, the 2D method costs about 20 CPU hours, and the 3D method needs more than 1500 CPU hours.
- (2) The 1D method agrees well with the 3D method under various rotational speeds and inlet pressures. The output power caused by the pressure obtained by the 2D method agrees with the 3D method, but the 2D method neglects friction loss on the top side and the bottom side.
- (3) A performance map of the turbine is generated using the corrected deviation between the 1D and 3D methods. The influence of system parameters on the performance of the turbine has been investigated using the performance map. A certain subcooling degree is beneficial for the design and the operation of the turbine.
- (4) The flow parameters along the channel evaluated by the 1D method agree with the average 3D flow in the channel. The 2D method can evaluate the nonuniform characteristic in the rotational direction, for example, the attachment of the liquid on the pressure side and the suction side.
- (5) The 1D method is an effective tool for fast evaluation of the performance map. The 2D method can provide more detail flow information especially the nonuniform flow in the rotational direction. The 3D method can fully illustrate the 3D flow and the performance of the turbine. But it also requires a huge number of computational resources and time. The presented 1D, 2D and 3D evaluation of the two-phase turbine can be applied to the geothermal system, but also the other systems including oil production, refrigeration, seawater desalination, and so on.

Table 5
Advantages and disadvantages of different methods.

Method	Advantages	Disadvantages
1D method	<ol style="list-style-type: none"> 1. Low time cost 2. High accuracy in predicting m, P_o, η and P_{o_f} 	<ol style="list-style-type: none"> 1. Low accuracy under various T_m and Q_m 2. P_o is evaluated by using the simple radial equilibrium 3. The accuracy of predicting P_{o_f} is constrained by the empirical model of the fictional two-phase pressure reduction
2D method	<ol style="list-style-type: none"> 1. Medium time cost 2. High accuracy in predicting X_g^{out} and P_{o_p} 3. Reflect the non-uniform flow in the rotational direction 	<ol style="list-style-type: none"> 1. Low accuracy in predicting m, P_o and P_{o_f} 2. Cannot reflect wall effects of the top side and bottom side 3. Cannot be applied under the low inlet pressure working condition
3D method	<ol style="list-style-type: none"> 1. High accuracy 	<ol style="list-style-type: none"> 1. Large time cost

Author contributions

H.L. mainly contributes in methodology, investigation, CFD, flow analysis and original draft preparation; S.R. mainly contributes in mathematical models, model parameters and validation of CFD, flow analysis and draft review; Z.Y. mainly contributes in conceptualization, draft review and editing, project administration and funding acquisition. All authors have read and agreed to the published version of the manuscript.

CRedit authorship contribution statement

Hongyang Li: Conceptualization, Methodology, Software, Validation, Formal analysis, Investigation, Data curation, Writing – original draft, Visualization. **Sham Rane:** Software, Validation, Investigation, Writing – review & editing. **Zhibin Yu:** Conceptualization, Writing – review & editing, Supervision, Project administration, Funding acquisition.

Declaration of competing interest

The authors declare that they have no known competing financial interests or personal relationships that could have appeared to influence the work reported in this paper.

Acknowledgement

This research is supported by the Engineering and Physical Sciences Research Council (EP/P028829/1, EP/N020472/1, EP/R003122/1) in United Kingdom. Authors would like to thank Dr Abhijit Date, RMIT, Australia, for providing the reference turbine test data for development and validation of the CFD model. Authors would like to thank Dr. Wenguang Li, University of Glasgow, United Kingdom, for reviewing this paper. Authors would also like to thank Professor Li He, University of Oxford, United Kingdom, for providing suggestions about the design and the numerical simulation of the two-phase turbine.

Nomenclature

A	Area
A_{ia}	Interfacial area density
C_D	Drag coefficient
C_p	Specific heat capacity at constant pressure
D	Bubble diameter
F	Force
h_{int}	Heat transfer coefficient between liquid and vapour
H	Enthalpy
I	Renthalpy
Ja_T	Jakob number
k	Turbulence kinetic energy
L	Length
La	Laplace number
m	Mass flow rate
N	Rotational speed
Nu	Nusselt number
P	Pressure
Pe	Peclet number
P_o	Output power
P_{of}	Output power caused by the friction
P_{op}	Output power caused by the pressure
R	Radius
Re	Reynold number
T	Temperature
To	Torque

U	Circumferential speed
V	Absolute velocity
W	Relative velocity
x, y, z	Cartesian coordinate axes
X_g	Vapour mass fraction

Greek Symbols

α	Vapour volume fraction
γ	Relative flow angle
η	Efficiency
ν	Kinetic viscosity
ρ	Density
λ	Fitting coefficient
ϕ	Arbitrary parameter
Φ	Two-phase frictional pressure reduction factor
ω	Dissipation of turbulent energy

Superscripts

BS	Bottom side
CL	Center line
d	Drag
ex	External
g	Gravity
in	Inlet
int	Interphase
out	Outlet
PS	Pressure side
sat	Saturation
SS	Suction side
t	Turbulence
TS	Top side

Subscripts

f	Friction
i	Node index
l	Liquid
v	Vapour

References

- [1] A. Aali, N. Pourmahmoud, V. Zare, Exergoeconomic analysis and multi-objective optimization of a novel combined flash-binary cycle for Sabalan geothermal power plant in Iran, *Energy Convers. Manag.* 143 (2017) 377–390, <https://doi.org/10.1016/j.enconman.2017.04.025>.
- [2] P. Erfurt-Cooper, The importance of natural geothermal resources in tourism, in: *Proc. World Geotherm. Congr.* 2010, pp. 25–29. Bali, Indonesia, <https://www.geothermal-energy.org/pdf/IGASTandard/WGC/2010/3318.pdf>. (Accessed 1 January 2021).
- [3] H.D. Madhawa Hettiarachchi, M. Golubovic, W.M. Worek, Y. Ikegami, Optimum design criteria for an Organic Rankine cycle using low-temperature geothermal heat sources, *Energy* 32 (2007) 1698–1706, <https://doi.org/10.1016/j.energy.2007.01.005>.
- [4] K. Wang, B. Yuan, G. Ji, X. Wu, A comprehensive review of geothermal energy extraction and utilization in oilfields, *J. Petrol. Sci. Eng.* 168 (2018) 465–477, <https://doi.org/10.1016/j.petrol.2018.05.012>.
- [5] M. Aneke, B. Agnew, C. Underwood, Performance analysis of the Chena binary geothermal power plant, *Appl. Therm. Eng.* 31 (2011) 1825–1832, <https://doi.org/10.1016/j.applthermaleng.2011.02.028>.
- [6] Z. Salameh, in: Z.B.T.-R.E.S.D. Salameh (Ed.), Chapter 5 - Emerging Renewable Energy Sources, Academic Press, Boston, 2014, pp. 299–371, <https://doi.org/10.1016/B978-0-12-374991-8.00005-2>.
- [7] S.-M. Lu, A global review of enhanced geothermal system (EGS), *Renew. Sustain. Energy Rev.* 81 (2018) 2902–2921, <https://doi.org/10.1016/j.rser.2017.06.097>.
- [8] A. Coskun, A. Bolatturk, M. Kanoglu, Thermodynamic analysis and optimization of various power cycles for a geothermal resource, *Energy Sources, Part A Recover. Util. Environ. Eff.* 38 (2016) 850–856, <https://doi.org/10.1080/15567036.2013.805285>.
- [9] S. Jalilinasrabad, R. Itoi, Flash cycle and binary geothermal power plant optimization, in: *Geotherm. Resour. Counc. Annu. Meet. GRC 2012 - Geotherm., Reno, NV, United States, 2012*, pp. 1079–1084, 2012.
- [10] Y. Cerci, Performance evaluation of a single-flash geothermal power plant in

- Denizli, Turkey, Energy 28 (2003) 27–35, [https://doi.org/10.1016/S0360-5442\(02\)00093-2](https://doi.org/10.1016/S0360-5442(02)00093-2).
- [11] N. Yildirim Ozcan, G. Gokcen, Thermodynamic assessment of gas removal systems for single-flash geothermal power plants, Appl. Therm. Eng. 29 (2009) 3246–3253, <https://doi.org/10.1016/j.applthermaleng.2009.04.031>.
- [12] V. Zare, V. Palideh, Employing thermoelectric generator for power generation enhancement in a Kalina cycle driven by low-grade geothermal energy, Appl. Therm. Eng. 130 (2018) 418–428, <https://doi.org/10.1016/j.applthermaleng.2017.10.160>.
- [13] M. Senturk Acar, O. Arslan, Energy and exergy analysis of solar energy-integrated, geothermal energy-powered Organic Rankine Cycle, J. Therm. Anal. Calorim. 137 (2019) 659–666, <https://doi.org/10.1007/s10973-018-7977-1>.
- [14] Z. Guzović, P. Rašković, Z. Blatarić, The comparison of a basic and a dual-pressure ORC (organic rankine cycle): geothermal power plant Velika Ciglena case study, Energy 76 (2014) 175–186, <https://doi.org/10.1016/j.energy.2014.06.005>.
- [15] I.K. Smith, Development of the trilateral flash cycle system: part 1: fundamental considerations, Proc. Inst. Mech. Eng. Part A J. Power Energy. 207 (1993) 179–194, https://doi.org/10.1243/PIME_PROC_1993_207_032_02.
- [16] H.E. Kimmel, S. Catherly, Thermo-fluid dynamics and design of liquid-vapour two-phase LNG expanders, in: Gas Process. Assoc. Tech. Meet. Adv. Process Equipment, 2010, Paris, Fr., Paris, France.
- [17] L. Hays, History and overview of two-phase flow turbines, in: IMECHE Conf. Trans., Mechanical Engineering Publications, 1999, pp. 159–170.
- [18] T. He, C. Xia, Y. Zhao, L. Li, P. Shu, An experimental study on energy recovery by a pelton-type expander in a domestic refrigeration system, HVAC R Res. 15 (2009) 785–799.
- [19] S.-Y. Cho, C.-H. Cho, C. Kim, Performance characteristics of a turbo expander substituted for expansion valve on air-conditioner, Exp. Therm. Fluid Sci. 32 (2008) 1655–1665, <https://doi.org/10.1016/j.expthermflusc.2008.05.007>.
- [20] W.J. Comfort III, Performance of a total-flow impulse turbine for geothermal applications, in: Twelfth Intersoc. Energy Convers. Eng. Conf., La Grance, Illinois, American Nuclear Society., Washington, D.C., 1977, pp. 893–898.
- [21] H. Li, S. Rane, Z. Yu, G. Yu, An inverse mean-line design method for optimizing radial outflow two-phase turbines in geothermal systems, Renew. Energy 168 (2021) 463–490, <https://doi.org/10.1016/j.renene.2020.12.079>.
- [22] D.G. Elliot, Theory and Tests of Two-phase Turbines, Jet Propulsion Laboratory, 1982, <https://doi.org/10.2172/5346135>.
- [23] D.G. Elliott, E. Weinberg, Acceleration of Liquids in Two Phase Nozzles, Pasadena, California, United States, 1968. <https://ntrs.nasa.gov/search.jsp?R=19680017730>. (Accessed 1 January 2021).
- [24] W.J. Comfort III, The Design and Evaluation of a Two-phase Turbine for Low Quality Steam-Water Mixtures, University of California, 1977.
- [25] W.J. Comfort III, C.W. Beadle, Design considerations for a two-phase turbine, in: Symposium on Polyphase Flow in Turbomachinery, ASME Winter Annual Meeting, San Francisco, California, n.d.
- [26] L.G. Hays, J.J. Brasz, Two-phase-flow turbines as stand-alone throttle replacement units in large 2000–5000 ton centrifugal chiller installations, in: Proc. 1998 Int. Compress. Eng. Conf. Purdue, Purdue University, West Lafayette, IN, United States, 1998, pp. 792–802.
- [27] L.G. Hays, J.J. Brasz, Two-phase turbines for compressor energy recovery, in: Proc. 1996 Int. Compress. Eng. Conf. Purdue Univ., Purdue University, West Lafayette, IN, United States, 1996.
- [28] H. Li, W. Li, X. Zhang, Y. Zhu, Z. Zuo, H. Chen, Design method of a two-phase annular nozzle in cryogenic liquid expander, Proc. Inst. Mech. Eng. Part A J. Power Energy. 233 (2019) 762–772, <https://doi.org/10.1177/0957650918822943>.
- [29] K. Akagawa, T. Fujii, J. Ohta, K. Inoue, K. Taniguchi, Performance characteristics of divergent-convergent nozzles for subcooled hot water, JSME Int. Journal. Ser. 2, Fluids Eng. Heat Transf. Power, Combust. Thermophys. Prop. 31 (1988) 718–726.
- [30] K. Akagawa, T. Fujii, S. Takagi, M. Takeda, K. Tsuji, Performance of Hero's turbine using two-phase mixture as working fluid: experimental results in an air-water two-phase system, Bull. JSME. 27 (1984) 2795–2802.
- [31] Y. Zhao, A. Akbarzadeh, J. Andrews, Simultaneous desalination and power generation using solar energy, Renew. Energy 34 (2009) 401–408, <https://doi.org/10.1016/j.renene.2008.05.018>.
- [32] A. Date, S. Vahaji, J. Andrews, A. Akbarzadeh, Experimental performance of a rotating two-phase reaction turbine, Appl. Therm. Eng. 76 (2015) 475–483, <https://doi.org/10.1016/j.applthermaleng.2014.11.039>.
- [33] S. Rane, L. He, CFD analysis of flashing flow in two-phase geothermal turbine design, J. Comput. Des. Eng. 7 (2020) 238–250, <https://doi.org/10.1093/jcde/qwaa020>.
- [34] S. Rane, L. He, Numerical analysis of a novel two-phase turbine using thermal non-Equilibrium, homogeneous nucleation phase change, Therm. Sci. Eng. Proc. 22 (2021), 100827, <https://doi.org/10.1016/j.tsep.2020.100827>.
- [35] H.M. Crockett, J.S. Horowitz, Erosion in Nuclear Piping Systems, vol. 132, J. Press. Vessel Technol., 2010, <https://doi.org/10.1115/1.4000509>.
- [36] J. Horowitz, Recommendations for Controlling Cavitation, Impingement Erosion, and Solid Particle Erosion in Nuclear Power Plant Piping Systems, 2004. Palo Alto, CA.
- [37] N.K. Singh, A.S.M. Ang, D.K. Mahajan, H. Singh, Cavitation erosion resistant nickel-based cermet coatings for monel K-500, Tribol. Int. 159 (2021), 106954, <https://doi.org/10.1016/j.triboint.2021.106954>.
- [38] J.F. dos Santos, C.M. Garzón, A.P. Tschiptschin, Improvement of the cavitation erosion resistance of an AISI 304L austenitic stainless steel by high temperature gas nitriding, Mater. Sci. Eng. 382 (2004) 378–386, <https://doi.org/10.1016/j.msea.2004.05.003>.
- [39] Y. Xi, D. Liu, D. Han, Improvement of corrosion and wear resistances of AISI 420 martensitic stainless steel using plasma nitriding at low temperature, Surf. Coating. Technol. 202 (2008) 2577–2583, <https://doi.org/10.1016/j.surfcoat.2007.09.036>.
- [40] A. Date, A. Khaghani, J. Andrews, A. Akbarzadeh, Performance of a rotating two-phase turbine for combined power generation and desalination, Appl. Therm. Eng. 76 (2015) 9–17, <https://doi.org/10.1016/j.applthermaleng.2014.08.074>.
- [41] Y. Liao, D. Lucas, A review on numerical modelling of flashing flow with application to nuclear safety analysis, Appl. Therm. Eng. 182 (2021), 116002, <https://doi.org/10.1016/j.applthermaleng.2020.116002>.
- [42] S. Rane, L. He, H. Ma, CFD modelling and analysis of two-phase geothermal energy turbine in project combi-gen, in: Int Conf Innov. Appl. Energy, 2019, p. 257, <https://doi.org/10.1093/jcde/qwaa020>. Oxford.
- [43] G. Yu, Z. Yu, Investigation of geothermally sourced combined power and freshwater generation systems, Energy Procedia 158 (2019) 5946–5953, <https://doi.org/10.1016/j.egypro.2019.01.527>.
- [44] H. Geremew, A Study of Thermodynamic Modelling and Gas Extraction System Design for Aluto Langanoo Geothermal Power Plant II in Ethiopia, Reykjavik, Iceland, 2012. <https://raflhadan.is/bitstream/handle/10802/8605/UNU-GTP-2012-10.pdf?sequence=1>.
- [45] G. Yu, Z. Yu, Research on a coupled total-flow and single-flash (TF-SF) system for power and freshwater generation from geothermal source, Appl. Sci. 10 (2020) 2689, <https://doi.org/10.3390/app10082689>.
- [46] M. Pollet, L. Gosselin, J. Dallaire, F. Mathieu-Potvin, Optimization of geothermal power plant design for evolving operating conditions, Appl. Therm. Eng. 134 (2018) 118–129, <https://doi.org/10.1115/1.4025570>.
- [47] M. Borremans, Pumps and Compressors, John Wiley & Sons, 2019, <https://doi.org/10.1002/9781119534112>.
- [48] R.H. Aungier, Turbine Aerodynamics: Axial-Flow and Radial-Flow Turbine Design and Analysis, ASME Press, 2006, <https://doi.org/10.1115/1.802418>.
- [49] S.L. Dixon, C. Hall, Fluid Mechanics and Thermodynamics of Turbomachinery, Butterworth-Heinemann, 2014, <https://doi.org/10.1016/C2011-0-05059-7>.
- [50] S.A. Korpela, Principles of Turbomachinery, Wiley Online Library, 2011, <https://doi.org/10.1002/9781118162477>.
- [51] E.J. Logan, R. Roy, Handbook of Turbomachinery, Marcel Dekker, Inc., New York, 2003, <https://doi.org/10.1201/9780203911990>.
- [52] R. Van den Braembussche, Design and Analysis of Centrifugal Compressors, ASME Press, 2020, <https://doi.org/10.1115/1.861VAN>.
- [53] Y.V. Fairuzov, Blowdown of pipelines carrying flashing liquids, AIChE J. 44 (1998) 245–254, <https://doi.org/10.1002/aic.690440203>.
- [54] S. Rane, L. He, Two-phase flow analysis and design of geothermal energy turbine, in: IOP Conf. Ser. Mater. Sci. Eng. IOP Publishing, 2019, p. 12043, <https://doi.org/10.1088/1757-899X/604/1/012043>.
- [55] K. Wolfert, The simulation of blowdown processes with consideration of thermodynamic non-equilibrium phenomena, in: Proc. Spec. Meet. Transient Two-phase Flow, OECD/Nuclear Energy Agency, Toronto, ON, Canada, 1976.
- [56] L. Cheng, Frontiers and Progress in Multiphase Flow I, Springer, 2014, https://doi.org/10.1007/978-3-319-04358-6_4.
- [57] R.W. Lockhart, R.C. Martinelli, Proposed correlation of data for isothermal two-phase, two-component flow in pipes, Chem. Eng. Prog. 45 (1949) 39–48. [http://dns2.asia.edu.tw/~ysho/YSHO-english/1000 CE/PDF/Che Eng Pro45, 39. pdf](http://dns2.asia.edu.tw/~ysho/YSHO-english/1000%20CE/PDF/Che%20Eng%20Pro45_39.pdf).
- [58] M.A. Woldesemayat, A.J. Ghajar, Comparison of void fraction correlations for different flow patterns in horizontal and upward inclined pipes, Int. J. Multiphas. Flow (2007) 347–370, <https://doi.org/10.1016/j.ijmultiphaseflow.2006.09.004>.
- [59] H. Yaonan, The governing equations and turbulence models of compressible turbulent flow in a rotating frame, J. Aero. Power 5 (1990) 239–244, 286. file:///jasp_cn/article/abstract/19900312.
- [60] I. Ansys, CFX-solver Theory Guide, Ansys, Canonsburg, 2018. https://ansyshelp.ansys.com/account/secured?returnurl=/Views/Secured/corp/v202/en/cfx_thry/cfx_thry.html. (Accessed 1 January 2021).
- [61] F.A. Lyman, On the conservation of rothalpy in turbomachines, J. Turbomach. 115 (1993) 520–525, <https://doi.org/10.1115/1.2929282>.
- [62] K. Ibrahim, W.A. El-Askary, A. Balabel, I.M. Sakr, Simulation of bubbly flow using different turbulence models, Comput. Model. Eng. & Sci. 85 (2012), <https://doi.org/10.3970/cmcs.2012.085.079>.
- [63] C.-H. Wu, A General Theory of Two-And Three-Dimensional Rotational Flow in Subsonic and Transonic Turbomachines, National Aeronautics and Space Administration, Scientific and Technical Information Program, Washington, DC, United States, 1993.
- [64] A. Khaghani, Dual Thermal System for Power and Fresh Water Production, RMIT University, 2013. <https://researchrepository.rmit.edu.au/esploro/outputs/doctoral/Dual-thermal-system-for-power-and-fresh-water->

- [production/9921861234401341#files_and_links](#). (Accessed 24 March 2021).
- [65] Y. Zhao, Combined Desalination and Power Generation Using Solar Energy, RMIT University, 2009. <https://researchrepository.rmit.edu.au/esploro/outputs/doctoral/Combined-desalination-and-power-generation-using-solar-energy/9921859083701341>. (Accessed 24 March 2021).
- [66] G.L. Dittman, Calculation of brine properties, United States, <https://doi.org/10.2172/7111583>, 1977.
- [67] Z. Woube, Analysis of Well Test Data from the Langano-Aluto Geothermal Field, Ethiopia, UNU-GTP, Iceland, 1986. <https://orkustofnun.is/gogn/unu-gtp-report/UNU-GTP-1986-11.pdf>.
- [68] E.M. Greitzer, C.S. Tan, M.B. Graf, Internal Flow: Concepts and Applications, Cambridge University Press, Cambridge, 2007.